Earth Syst. Sci. Data, 18, 8107–8127, 2026
https://doi.org/10.5194/essd-18-8107-2026
© Author(s) 2026. This work is distributed under
the Creative Commons Attribution 4.0 License.

Open Access Earth System Science Data

Age of smoke sampled by aircraft during FIREX-AQ: methods and critical evaluation

Christopher D. Holmes[1], Joshua P. Schwarz[2], Charles H. Fite[1,a,b], Anxhelo Agastra[1], Holly K. Nowell[1,c], Katherine Ball[2,d], T. Paul Bui[3], Jonathan Dean-Day[4], Zachary C. J. Decker[5,2], Joshua P. DiGangi[6], Glenn S. Diskin[6], Emily M. Gargulinski[7,6], Hannah Halliday[6,e], Shobha Kondragunta[8], John B. Nowak[6], David A. Peterson[9], Michael A. Robinson[5,2], Amber J. Soja[6], Rebecca A. Washenfelder[2], Chuanyu Xu[10], and Robert J. Yokelson[11]

[1]Department of Earth, Ocean and Atmospheric Science, Florida State University, Tallahassee, Florida, USA
[2]NOAA Chemical Sciences Laboratory, Boulder, Colorado, USA
[3]NASA Ames Research Center, Moffett Field, California, USA
[4]Bay Area Environmental Research Institute, Moffett Field, California, USA
[5]Cooperative Institute for Research in Environmental Sciences, University of Colorado, Boulder, Colorado, 80309, USA
[6]NASA Langley Research Center, Hampton, Virginia, USA
[7]National Institute of Aerospace, Hampton, Virginia, USA
[8]NOAA/NESDIS, College Park, Maryland, USA
[9]Naval Research Laboratory, Monterey, California, USA
[10]I. M. Systems Group at NOAA, College Park, Maryland, USA
[11]Department of Chemistry, University of Montana, Missoula, Montana, USA
[a]now at: Cooperative Institute of Satellite Earth System Studies (CISESS), Center for Spatial Information Science and Systems, George Mason University, Fairfax, VA, USA
[b]now at: NOAA Air Resources Laboratory, College Park, Maryland, USA
[c]now at: Tall Timbers Research Station and Land Conservancy, Tallahassee, Florida, USA
[d]now at: California Institute of Technology, Pasadena, California, USA
[e]now at: United States Environmental Protection Agency, Office of Research and Development, Durham, North Carolina, USA

Correspondence: Christopher D. Holmes (cdholmes@fsu.edu)

Received: 23 May 2025 – Discussion started: 24 June 2025
Revised: 25 September 2026 – Accepted: 8 October 2026 – Published: 5 November 2026

Abstract. The age of smoke, meaning the time elapsed since it was produced in a fire, is an important parameter for interpreting measurements of evolving smoke composition. This study describes the smoke age estimates developed for large plumes sampled in the 2019 NASA-NOAA FIREX-AQ field experiment. Smoke ages are computed using two methods and applied to observations from two aircraft: the NASA DC-8 and NOAA Chemistry Twin Otter. The first method uses measurements of mean horizontal wind speed, as observed by the sampling aircraft, and distance to the fire to provide a single age estimate for each plume-crossing performed by the aircraft. While this "mean-wind method" uses accurate wind measurements, it can be systematically biased by assumptions that plume rise time is negligible and that winds are homogeneous horizontally and in time during the plume transport. Wind inhomogeneities due to terrain effects and day-to-night transition, among other factors, affected some plumes during FIREX-AQ. The mean-wind method therefore performs best for short-range transport over level terrain with steady winds. The second method relies on upwind air parcel trajectories and plume rise computed with multiple high-resolution meteorological datasets. This "trajectory-based method" quantifies age uncertainty from the meteorological ensemble, plume rise speed, wind speed errors, and fire location. The second method also resolves age differences from the center to edge of a transect. Still, it is susceptible

to errors in the meteorological model. With careful comparison of the simulated trajectories to smoke transport observed from geostationary satellite imagery described here, we filter out many trajectory errors and improve the smoke age estimates. Across the two aircraft, the dataset provides ages for over 43 h (815 transects) of in situ measurements in smoke plumes from 115 different fires, with smoke ages ranging from 1 min to 40 h. The two age methods are strongly correlated ($R = 0.89$) for the periods during FIREX-AQ when both ages are available. The mean-wind age is systematically 12 % younger than the trajectory-based age and the median absolute difference between them is 15 % (21 % for mean). The favorable agreement between the two age methods reflects that the mean-wind method was selectively applied to plumes with little wind variability. Trajectory-based ages are available for more of the FIREX-AQ smoke observations than the mean-wind ages. The median trajectory-based age uncertainty during FIREX-AQ is 24 % and the mean uncertainty is 37 %, due to a long-tailed distribution. The main source of age uncertainty is spread within the meteorological ensemble, followed by discrepancy between measured and modeled wind speed, then other factors like plume rise. The age uncertainty variable enables the user to identify periods with high or low confidence in the age estimate, thereby informing studies of smoke aging. Smoke ages data are available at https://doi.org/10.5067/ASDC/FIREXAQ_MetNav_ AircraftIn-Situ_DC8_Data_1 (Bennett et al., 2020) for the NASA DC-8 and https://doi.org/10.5067/ASDC/SUBORBITAL/FIREXAQ_Analysis_N48_Data_1 (Holmes, 2021a) for the NOAA Chemistry Twin Otter.

1 Introduction

The NASA-NOAA Fire Influence on Regional to Global Environments and Air Quality (FIREX-AQ) campaign extensively sampled smoke from wildfires and prescribed fires over the United States in July through September 2019 (Warneke et al., 2023). Two participating aircraft focused on in situ measurements of smoke composition: the NASA DC-8 and NOAA Chemistry Twin Otter. They contained multiple instruments for measuring the chemical, physical, and optical properties of trace gases and aerosol in smoke. Understanding the chemical and physical evolution of the smoke from these measurements requires knowing the physical age of the smoke, meaning time elapsed since its emission at the fire source.

Determining the time for air parcel transport from a source location to a measurement location is an old problem in atmospheric science (see reviews by Fleming et al., 2012; Stohl, 1998). Over short periods of time when winds are steady (often 1–3 h or less), the transport time from an upwind source to a downwind receptor can be determined from the wind speed and distance (e.g. Pueschel and Van Valin, 1978; Ryerson et al., 1998; Yokelson et al., 2003). When winds are variable, which almost inevitably occurs on time scales of hours and longer, Lagrangian air parcel trajectory calculations that account for the evolving wind field are needed. HYSPLIT (Hybrid Single-Particle Lagrangian Integrated Trajectory) and FLEXTRA (FLEXible TRAjectories) are two widely used trajectory models (Stein et al., 2015; Stohl et al., 1995), among many others (Fleming et al., 2012; Stohl, 1998). Buoyant plume rise, as occurs in fires and some industrial sources (Briggs, 1969; Freitas et al., 2007), introduces additional complications to determining the transport time, as buoyant vertical motions are typically not resolved in large-scale meteorological datasets used to drive trajectory calculations. The level of accuracy required for plume age estimates depends on the application, as age uncertainties propagate to inferred rates and timescales of chemical processing. Studies of rapid chemical evolution in young plumes (< 1 h) may require age uncertainties below $\sim$5–10 min, whereas analyses of more aged plumes or broader trends in composition may tolerate larger uncertainties. Studies linking downwind smoke properties to fuel and fire conditions at the source may need accuracy $\sim$ 1–3 h, reflecting the timescale over which fire behavior often evolves across the diurnal cycle.

This work describes the methods and resulting dataset of smoke age for the FIREX-AQ campaign. Section 2 explains two methods used for computing ages: one based on measured mean wind speed and another based on an ensemble of air parcel trajectories. Geostationary satellite imagery is used to screen the trajectory ensemble and exclude implausible trajectories from the smoke age calculation. Innovative aspects of this work are the inclusion of plume rise and thorough accounting of age uncertainty in the trajectory-based method. Section 3 evaluates smoke age estimates from the two methods, examines the contribution of plume rise to smoke age, and analyzes uncertainties in the ages. Section 4 describes the data availability and Sect. 5 provides conclusions and implications.

2 Data and methods

2.1 Aircraft data and smoke plume identification

This work examines the age of smoke sampled in situ by two aircraft during FIREX-AQ: the NASA DC-8 and NOAA Chemistry Twin Otter (NOAA48). The NASA ER-2 and a second NOAA Twin Otter (NOAA46) that collected remote sensing measurements will not be discussed here. Both the

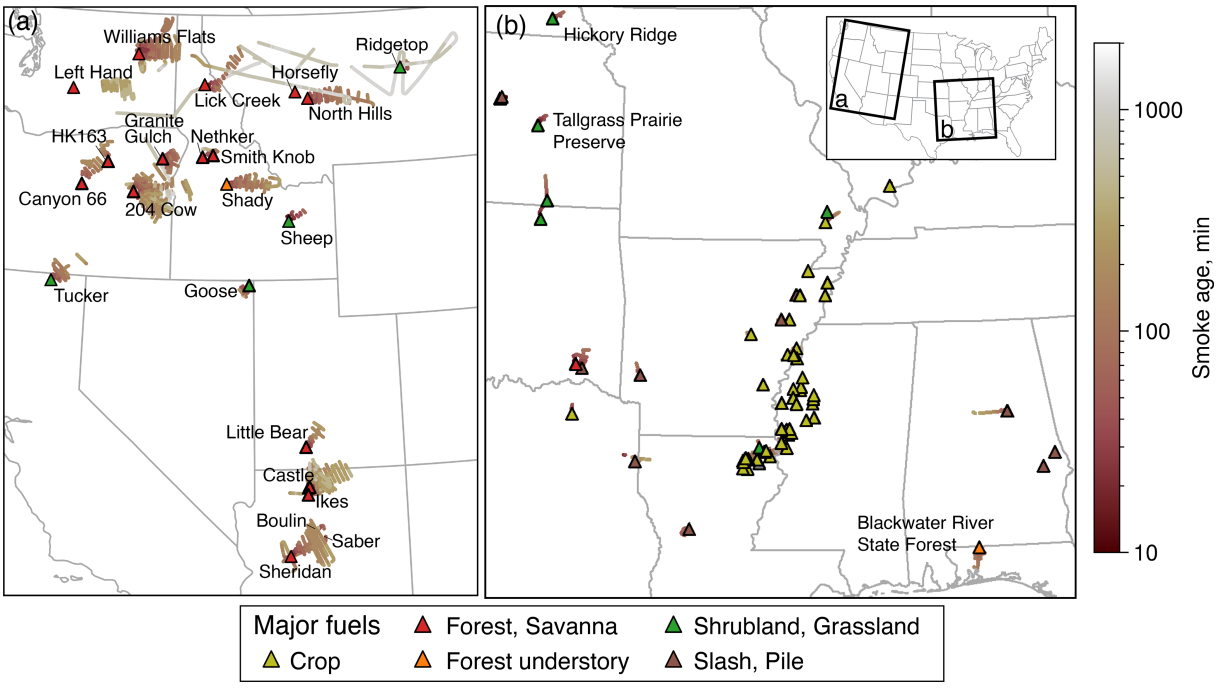


Figure 1. Map of fires (triangles, colored by major fuels) and smoke age (colored shading) sampled by the NASA DC-8 and NOAA Chemistry Twin Otter during FIREX-AQ, as estimated by the trajectory-based method. Panels show the **(a)** western US and **(b)** eastern US. The inset map shows the location of each panel within the contiguous US.

DC-8 and Twin Otter intercepted numerous smoke plumes at multiple distances and ages downwind of the source fires, as shown in Fig. 1. Smoke encounters are identified by manually inspecting the time series of measured carbon monoxide (CO, both aircraft) and black carbon aerosol (DC-8 only) for periods of elevated concentrations above the local background. The DC-8 instruments used to identify smoke are Differential Absorption Carbon monOxide Measurements (DACOM) for CO (Sachse et al., 1991) and Single Particle Soot Photometer (SP2) for black carbon (Schwarz et al., 2008). For the Twin Otter, a near-infrared cavity ring-down spectrometer is used for CO (Crosson, 2008; Karion et al., 2013). Each passage of an aircraft through a smoke plume is referred to as a transect. Most plume transects were crosswind (i.e. transverse), meaning the aircraft flew nearly perpendicular to the local wind, or along-wind (i.e. longitudinal), meaning nearly parallel to the wind, while some had other or unclear wind orientation, such as when winds were light or variable or when the transect was almost directly above the fire. The start and end times of each plume transect are determined to the nearest second.

Smoke age is estimated for all in situ smoke measurements in which the source fire could be identified. This includes smoke from 15 western US wildfires sampled by the DC-8 (24 July–16 August 2019), 11 western wildfires sampled by the Twin Otter (20 July–5 September 2019), and 89 central and eastern US fires sampled by the DC-8 (21 August–3 September 2019). The eastern US fires include larger prescribed fires in the Blackwater River State Forest (Florida), Hickory Ridge Wildlife Management Area (Nebraska), and Tallgrass Prairie Preserve (Kansas), along with many smaller crop and timber slash fires. For some transects, the age is estimated with only one method for reasons discussed in Sect. 2.3. Table A1 summarizes the fires and smoke transects with smoke age estimates.

2.2 Fire locations

Most smoke plumes sampled by the DC-8 and Twin Otter during FIREX-AQ were visually traceable to a single fire or fire complex by personnel on board the aircraft. These fires ranged in size from < 1 km across to about 15 km, with 1–4 km being common. For plumes sampled by the Twin Otter, precise locations of the source fires are determined from Moderate Resolution Imaging Spectroradiometer (MODIS) and Visible Infrared Imaging Radiometer Suite (VIIRS) active fire detections on the flight day. The centroid (latitude, longitude, and altitude) of the active fire pixels is used as the source for smoke age calculations. On some days, the satellite instruments did not detect the fires that were sampled by aircraft, which can occur because of clouds, small fire size, or burning that did not coincide with a satellite overpass. In these cases, we take the fire location from satellite detections on surrounding days or, if those are also unavailable, from fire incident reports (National Interagency Coordination Center, 2019). For plumes sampled by the DC-8, precise source

fire locations are determined from infrared imagery collected by the onboard MODIS/ASTER Airborne Simulator instrument (MASTER; Hook et al., 2001). MASTER provides fire temperature and fire radiative power at a horizontal resolution that depends on aircraft altitude, typically ∼ 10-m-scale for the fires examined here. From the DC-8 overpass that provided the most complete MASTER image of each fire, the fire centroid is calculated using fire radiative power as an averaging weight. Smoke age calculations treat the fire as a point source at the centroid location, with special accommodations for the largest fires described below.

The fire locations used in smoke age calculations are updated each flight day to account for fire movement over multiple days. For example, the flame front of the Castle Fire moved 1.8 km from 13 to 14 August, when it was sampled by the DC-8, and 5 km by 22 August, when it was sampled by the Twin Otter. The two largest fire complexes sampled during FIREX-AQ – the Williams Flats (18 000 ha) and Sheep (45 000 ha) Fires – had multiple centers of fire activity that produced multiple, distinct smoke plumes separated by over 10 km. For these very large fires, separate source locations are determined for each fire center and matched to downwind plume transects. A few plume transects contain mixtures of smoke from multiple fires or the source fire cannot be identified confidently. In these cases, all potential source fire locations are used and the uncertainty in smoke age accounts for ambiguity in the source location (Sect. 2.4). More generally, smoke from a mixture of sources can be considered to have a spectrum of ages, but FIREX-AQ aircraft rarely sampled such mixtures, so the approach of providing a single age with uncertainty is used here.

2.3 Smoke age from measured wind profiles: "mean-wind age"

The first method for calculating smoke age relies on in situ wind measurements from the aircraft, as a long-established approach (e.g. Akagi et al., 2012; Pueschel and Van Valin, 1978; Ryerson et al., 1998; Yokelson et al., 2003). We refer to this as the "mean-wind age." A vertical profile of mean wind speed is calculated from all in situ wind measurements during the flight within 3° (latitude and longitude) of the fire. These wind measurements are averaged into 1000 m vertical bins. A mean wind speed vertical profile is constructed for each fire sampled during each flight. The smoke age is then determined from the distance between the source fire and the downwind measurement location, divided by the mean wind speed interpolated to the measurement altitude. This assumes that upwind transport occurs at the measurement altitude and that the plume's vertical rise time is small; both assumptions will be critically evaluated in Sect. 3. Observed wind variability within the domain used to construct the mean vertical profile might help constrain age uncertainty; however, this remains for future work. The mean-wind age is computed for all smoke plume transects with crosswind or along-wind orientations. For crosswind transects, the distance and age are calculated at the transect center and all measurements during that transect are assigned the same age. For along-wind transects, the distance and hence age are calculated from the aircraft location each second. No age is calculated for transects with other or unclear orientation to the wind. The wind measurements used in the mean wind age calculation come from the Meteorological Measurements System (MMS) instrument on the DC-8 (Scott et al., 1990). Wind measurements from the Twin Otter have quality issues that prevent their use, so mean wind age is provided only for DC-8 smoke samples. The mean-wind age is also not applied to smoke sampled by the DC-8 beyond about 200 km from a fire or for plumes with obvious wind shifts, as the assumption of constant wind profile would be violated. Table 1 lists the variables related to mean-wind age that are contained in the FIREX-AQ data archive.

2.4 Smoke age from wind trajectories: "trajectory-based age"

The second method for calculating smoke age uses upwind trajectories originating from the aircraft measurement locations and tracing back to the source fire. We refer to this as the "trajectory-based age" and compute it for all smoke with a known fire source. The method is applied to all smoke transects with a known source fire (regardless of wind orientation), so trajectory-based ages are available in many cases where the mean-wind age is not. Trajectories are initialized from the aircraft location at 5 s intervals during smoke sampling and propagated upwind using the NOAA HYSPLIT model (Stein et al., 2015). Three upwind trajectories are computed from each aircraft location using three meteorological datasets (Sect. 2.5). All trajectories extend 60 h upwind with intermediate trajectory positions recorded every 10 min.

We decompose the smoke age into two components: advection ($\tau_{\mathrm{adv},m}$) and buoyant plume rise ($\tau_{\mathrm{rise},m}$):

$$\tau_m = \tau_{\mathrm{adv},m} + \tau_{\mathrm{rise},m}. \quad (1)$$

Each of the meteorological datasets (m) provide an estimate of the age and its rise and advection components. The advection age ($\tau_{\mathrm{adv},m}$) is determined from the point when the upwind trajectory is closest to the source fire, as illustrated in Fig. 2. Plume rise is not always vertical, but this is reasonable for fires sampled in FIREX-AQ. In some cases, wind shifts cause the upwind trajectory to pass over the fire multiple times. In those cases, we assume that the youngest age is most likely. The buoyant rise component of plume age is determined by the altitude of the trajectory above ground at the point of closest approach ($z_{\mathrm{rise},m}$) and an empirical plume rise vertical speed (w_{rise}):

$$\tau_{\mathrm{rise},m} = z_{\mathrm{rise},m}/w_{\mathrm{rise}}. \quad (2)$$

Table 1. Smoke age variables contained in ICARTT files for FIREX-AQ.

Age method	Variable	Description, units
Mean-wind age		
	transect_smoke_age	Age of smoke at center of transect, s
	fire_distance_estimate	Distance from fire to center of transect, m
Trajectory-based age*		
	smoke_age (τ)	Age of smoke, s
	smoke_age_unc ($\delta\tau$)	Uncertainty in age of smoke, s
	smoke_age_corr (τ')	Age of smoke after scaling trajectory to match observed wind speed, s
	smoke_age_rise (τ_{rise})	Age of smoke due to plume rise to trajectory altitude, s
	smoke_rise (z_{rise})	Plume rise height from surface to trajectory altitude, m
	fire_distance	Distance from fire to aircraft, m
	smoke_age_method	Indicator for which meteorological datasets are used in the best age estimate; all datasets are used for uncertainties; 1 = HRRR,NAM,GFS (default); 2 = HRRR,NAM; 3 = HRRR,GFS; 4 = NAM,GFS; 5 = HRRR; 6 = NAM; 7 = GFS

* Symbols in parentheses are used in Sect. 2.4.

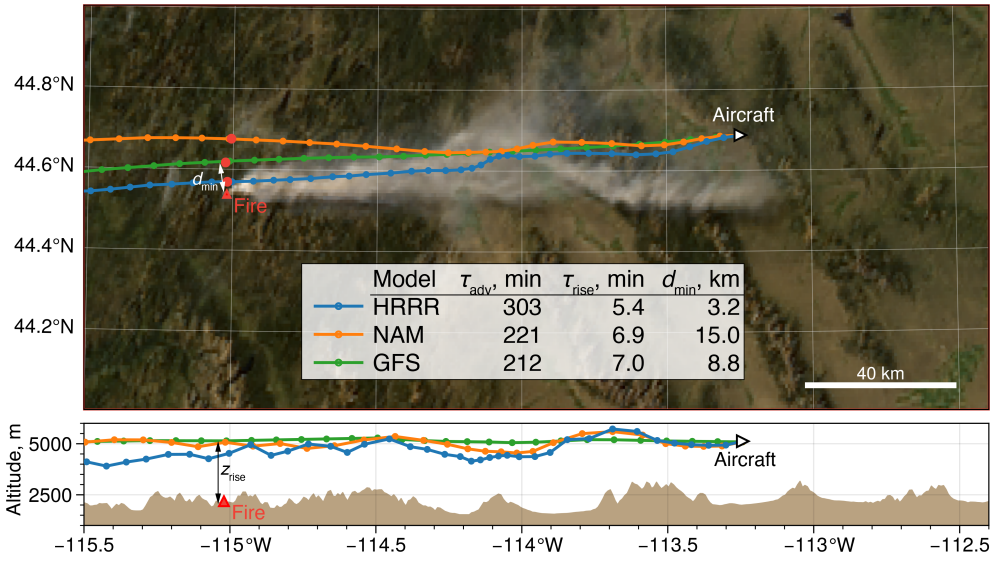


Figure 2. Example trajectories used for smoke age calculation, based on the Shady Fire, Idaho. Lines show upwind trajectories in three meteorological datasets, with dots marking 10 min intervals and a red dot marking the closest trajectory approach to the fire where the advection age is determined. The inset table gives the age contributions from advection (τ_{adv}) and plume rise (τ_{rise}), as well as the minimum separation between the trajectory and fire (d_{min}) for this example. The background image is a true color image from GOES-West (26 July 2019 00:21 UTC), including terrain parallax correction (Sect. 2.6). For the example shown, $\langle\tau_{\mathrm{adv},m}\rangle = 245$ min and $\langle\tau_{\mathrm{rise},m}\rangle = 6.4$ min, so the trajectory-based age estimate is $\tau = 251.4$ min.

Using upwind trajectories from the aircraft allows plume rise ($z_{\mathrm{rise},m}$) to be inferred from the trajectories, whereas downwind trajectories from the fire require prior information about plume rise. Measurements of updraft speeds in wildfire smoke plumes are limited to a few case studies, but nevertheless show that vertical velocities vary with altitude and fire conditions and often fluctuate rapidly (Clements et al., 2018; Lareau and Clements, 2017; Rodriguez et al., 2020). In a smoke column topped with pyrocumulus clouds, like those commonly observed during FIREX-AQ, updraft speeds have been observed decreasing from 13 to 7 m s^{-1} in the 2 km above a fire (Lareau and Clements, 2017). In a pyrocumulonimbus, median updraft speeds of 5–18 m s^{-1} have been observed, albeit with much larger extremes (Clements et al., 2018; Rodriguez et al., 2020). In a larger dataset of ordinary cumulonimbus, median updraft speeds of 4–7 m s^{-1} were observed and extremes (95th percentile) were about twice the median (Giangrande et al., 2013). In 1-D smoke plume mod-

els, updraft speeds around 3–8 $\mathrm{m\,s^{-1}}$ have been simulated for plumes extending to 3 km altitude and around 6–15 $\mathrm{m\,s^{-1}}$ for plumes that generate deep convection up to 8 km altitude (Freitas et al., 2007). Based on these studies, we compute plume rise time using an updraft speed of $7 \pm 3.5\,\mathrm{m\,s^{-1}}$ for plumes without clouds or with pyrocumulus. For a few plumes that generated pyrocumulonimbus (Williams Flats Fire, 8 August 2019) an updraft speed of $12 \pm 6\,\mathrm{m\,s^{-1}}$ is used in age calculations. For FIREX-AQ samples, a typical plume rise distance is around 2000 m and a typical rise time is thus around 5 min.

We plot and visually screen all simulated trajectories from all meteorological datasets for consistency with the plume transport seen in geostationary satellite imagery (Sect. 2.6). If a meteorological dataset yields trajectories grossly inconsistent with satellite-observed transport for a particular smoke transect, it is excluded from age analysis of that transect. Trajectories from the remaining meteorological datasets are considered equally plausible and used to determine the age. Examples of gross trajectory problems include wind directions errors exceeding 45°, wind speed errors exceeding 50 % of observed wind speed, and implausible wind shifts. One or more meteorological datasets is excluded for about 30 % of transects. A data variable named "smoke_age_method" indicates which meteorological datasets have been included or excluded for each time point in the smoke age dataset. Our best estimate of smoke age is

$$\tau = \langle \tau_m \rangle = \langle \tau_{\mathrm{adv},m} \rangle + \langle \tau_{\mathrm{rise},m} \rangle \quad (3)$$

where represents the ensemble mean of ages derived from meteorological datasets that produced plausible upwind trajectories. Since upwind trajectories are computed from the aircraft location every 5 s, the best smoke age is first calculated at this frequency, then linearly interpolated to a 1 s time basis for consistency with other aircraft measurements.

Inferred smoke ages are susceptible to errors in the meteorological analysis datasets. To constrain the magnitude of this effect, we compare the wind speed observed by the aircraft (u_o) to the model (u_m) at the aircraft location. If the observed wind speed is slower than the model predicts ($u_m/u_\mathrm{o} > 1$), then the smoke age may be greater than implied by the trajectory-based method. We therefore compute a second advection age $\tau'_{\mathrm{adv},m} = \tau_{\mathrm{adv},m}(u_m/u_\mathrm{o})$ and second smoke age $\tau'_m = \tau'_{\mathrm{adv},m} + \tau_{\mathrm{rise},m}$ for each observation within a transect. We refer to this as a wind speed correction, which is performed for each meteorological dataset m. Since wind speed errors at the aircraft measurement point may not be representative of wind speed errors along the entire upwind trajectory, the wind speed corrected ages are not necessarily more accurate, but they are useful for quantifying age uncertainty, as discussed in the next paragraph.

Estimates of uncertainty in smoke age are provided with each age estimate. The factors that influence this uncertainty include spread in age among the meteorological datasets, differences between measured and modeled wind speed, convective vertical velocity, and sometimes multiple potential source fires. These individual uncertainties (δ_i), defined as follows, are assumed to be independent and are therefore summed in quadrature to determine the overall age uncertainty: $\delta\tau = (\sum_i \delta_i^2)^{1/2}$.

1. Spread in advection age across the ensemble of meteorology datasets: $\delta_{\mathrm{adv,ens}} = s\{\tau_{\mathrm{adv},m}\}$. Here, $s\{x_m\}$ represents the sample standard deviation of variable x derived from multiple meteorological datasets m.

2. Spread in plume rise time across the ensemble of meteorology datasets: $\delta_{\mathrm{rise,ens}} = s\{\tau_{\mathrm{rise},m}\}$

3. Uncertainty in pyroconvective vertical velocity: $\delta_{\mathrm{rise,w}} = \langle \tau_{\mathrm{rise},m} \rangle \frac{\delta w_{\mathrm{rise}}}{w_{\mathrm{rise}}}$. As described above, $w_{\mathrm{rise}} \pm \delta w_{\mathrm{rise}}$ is $12 \pm 6\,\mathrm{m\,s^{-1}}$ for smoke lofted in pyrocumulonimbus and $7 \pm 3.5\,\mathrm{m\,s^{-1}}$ otherwise.

4. Wind speed error in meteorological datasets: $\delta_{\mathrm{ws}} = \frac{1}{2}\langle |\tau_{\mathrm{adv},m} - \tau'_{\mathrm{adv},m}| \rangle$. This term represents the spread between age estimates with and without wind speed correction, averaged across the ensemble of meteorological datasets.

5. Trajectory displacement from source fire: $\delta_{\mathrm{traj}} = \langle d_{\mathrm{min},m} \rangle^2 / (2 d_\mathrm{o} \langle u_m \rangle)$. An upwind trajectory that doesn't pass directly over the source fire could indicate an error in the smoke age derived from that trajectory. We use scale analysis to approximate the associated age uncertainty. At the point where the trajectory is closest to the fire, the minimum distance between them ($d_{\mathrm{min},m}$, Fig. 2) could be traversed in time $d_{\mathrm{min},m}/u_m$, where u_m is the wind speed along the trajectory. Long-distance upwind trajectories are always expected to accumulate more error than short trajectories, so the age error likely scales with the ratio $d_{\mathrm{min},m}/d_\mathrm{o}$, where d_o is the aircraft distance from the fire when the observation was made, which is also where the trajectory was initialized. We multiply these two scaling terms. The result is divided by 2 out of analogy that in a normal distribution the standard deviation is half of a result at the 95 % confidence interval.

6. Source fire ambiguity: $\delta_{\mathrm{source}} = \langle s_m\{\tau_{m,f}\} \rangle$. For smoke plumes with more than one possible source fire (Sect. 2.2), the smoke age $\tau_{m,f}$ was calculated for each possible source fire f. The quantity $s_m\{\tau_{m,f}\}$ represents the sample standard deviation of these possible ages within meteorology dataset m.

The smoke age uncertainty is quantified for each observation. As discussed in Sect. 3.4, the resulting uncertainty varies spatially and temporally between and within smoke

plume transects, identifying observations where the age can be determined with greater or lesser confidence.

Table 1 lists the variables related to trajectory-based age and age uncertainty that are contained in the FIREX-AQ data archive. All age computations, apart from the HYSPLIT trajectory calculations are done in Python. Cartopy is used for great circle distance calculations and mapping (Elson et al., 2018). The GNU Parallel utility is used to parallelize computing tasks (Tange, 2011).

2.5 Meteorological data and HYSPLIT developments

We use three meteorological datasets from NOAA to drive HYSPLIT in this work. These are High Resolution Rapid Refresh (HRRR; Dowell et al., 2022), North American Mesoscale Contiguous United States nest (NAM CONUS; Rogers et al., 2009), and Global Forecast System (GFS; NCEP, 2019, 2021). The HRRR and NAM models have 3 km horizontal resolution while GFS is 0.25°. In the vertical, winds and other meteorological variables are saved on the native grid of each model (not standard pressure levels). These are 36 levels for HRRR, 40 for NAM, and 55 for GFS, plus an additional layer of surface variables in each model. The NOAA Air Resources Laboratory (ARL) maintains a long-term archive of the HRRR and GFS products in the file format used by HYSPLIT. For NAM CONUS, we create our own archive by piecing together the first six forecast hours of four daily model initializations (00:00, 06:00, 12:00, 18:00Z). This is the same method that ARL uses for the HRRR, GFS and other archives that they maintain. On two days when the NAM CONUS was not archived (14 and 25 August 2019), we use the 12 km NAM in its place. The GFS and NAM data that we use are never more than 6 h after meteorological forecast initialization and HRRR is never more than one hour after initialization.

Trajectories are computed with HYSPLIT version 4.2 with the following improvements and bug fix. The trajectory output frequency and precision are increased to every 10 min of advection time. Capabilities are added to output wind speed and direction along the trajectory, which enables evaluation against the in situ aircraft wind measurements. We also correct the radius of Earth that HYSPLIT uses when handling HRRR and NAM data to match the value used in those meteorological models (6370.0 km). This geolocation error shifts the meteorological grid by up to 1 km.

2.6 Geostationary satellite images

To better understand smoke transport from the fire to the aircraft and provide context for the aircraft measurements, we process and use geostationary satellite imagery from Geostationary Operational Environmental Satellites (GOES): GOES-East (GOES-16) and GOES-West (GOES-17). True color images are derived from Advanced Baseline Imager (ABI) Level 2 Cloud and Moisture Imagery (CMIPC) blue (B, 0.47 µm), red (R, 0.64 µm), and near infrared (NIR, 0.86 µm) reflectance (GOES-R Algorithm Working Group; NOAA Geostationary Operation Environmental Satellite-R Series, 2017). The blue and near infrared channels (1 km nadir resolution) are sharpened to the red channel resolution (0.5 km nadir resolution) using the method from Miller et al. (2020). Since ABI does not have a green channel, a simulated green channel is constructed from a weighted average of the blue, red, and near infrared ($G = 0.45R + 0.45B + 0.1NIR$) (Bah et al., 2018; Mosher et al., 2023). The three channels are then combined into a true color image and contrast is increased in the dark to moderate values to brighten surfaces and accentuate differences between smoke and clouds (Bah et al., 2018). The resulting images are similar to other daytime true color products derived from ABI data (Mosher et al., 2023), while enabling easier distinction between clouds and smoke and providing more accurate surface locations, as described next. GOES images are available at 5 min time intervals over the contiguous United States.

Most software packages provide geolocations for GOES data by projecting the satellite image onto Earth's ellipsoid. While this provides the correct latitude and longitude for features at sea level, anything above sea level – including elevated land, clouds, and smoke – appears displaced from its true latitude and longitude (e.g. Akagi et al., 2012). This satellite parallax effect produces geolocation errors that increase with altitude and with distance from the sub-satellite point (Fig. 3). For terrain in the western US imaged by GOES-East, the naively projected locations are frequently 2–8 km north and west of the true location. In this work, the GOES images and image data provided in the FIREX-AQ data archive correct for the terrain parallax effect. Surface elevation data from a 30 arcsec (∼ 1 km) resolution dataset (GTOPO30; Gesch et al., 1999) are projected into the ABI geostationary perspective, which provides an interpolation map from the image pixel coordinates to accurate latitude-longitude geolocations on Earth's surface. Figure 3c illustrates a smoke plume in the uncorrected images that appears to originate from locations where there were no fires. With parallax correction (Fig. 3d), however, the smoke plumes begin over the fire locations. Clouds and smoke, which are above ground level, are still affected by the parallax effect, however. GOES-East and GOES-West images and movies (mp4 format) of all fires sampled during FIREX-AQ are available in the FIREX-AQ data archive. RGB image data on a regular latitude-longitude grid are also provided in netCDF format to enable users to combine these images with data of their choice.

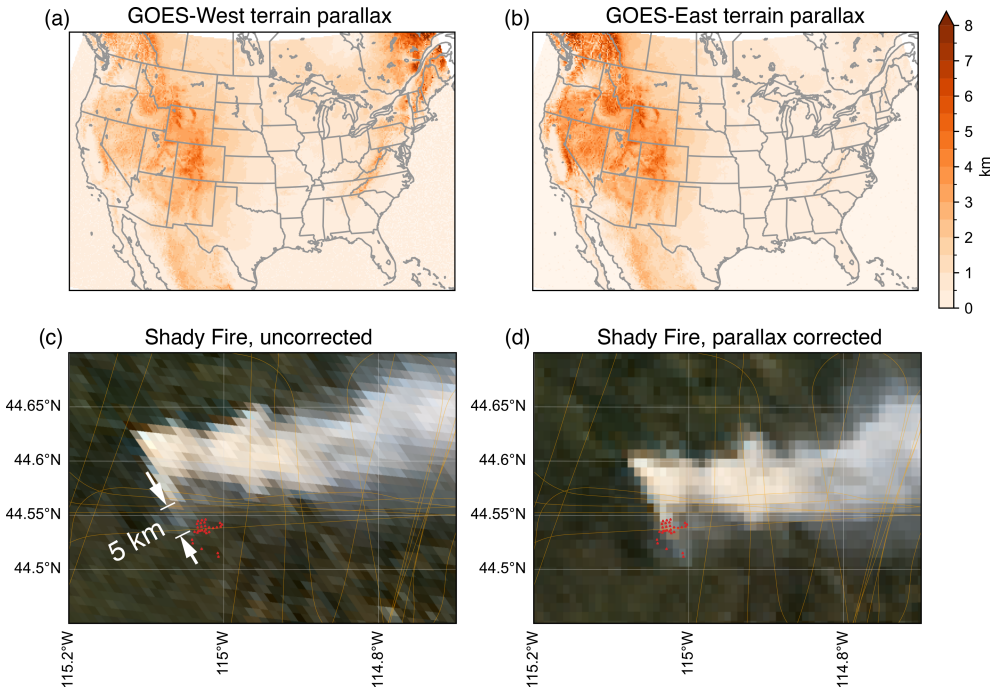


Figure 3. Terrain parallax effect for GOES-West **(a)** and GOES-East **(b)** over the contiguous United States with comparison of uncorrected **(c)** and corrected **(d)** images of the Shady Fire from GOES-East. The parallax effect in panels **(a)** and **(b)** is the offset distance between the apparent location of a surface feature and its actual location. The apparent smoke plume source in panel **(c)** is offset (white arrow) by nearly 5 km from the active fires (red dots, VIIRS active fires), while the two coincide in the corrected image in panel **(d)**. The GOES-East image was collected at 22:11 UTC on 25 July 2019.

Table 2. Statistical comparison of meteorological models to in situ measurements during smoke sampling in the western US by the NASA DC-8.

Variable	Model/instrument	Performance metrics		
		Bias	MAD	R
Wind speed, $m\,s^{-1}$	NAM CONUS	−0.02	1.28	0.89
	HRRR	0.25	1.40	0.87
	GFS (0.25°)	0.02	1.23	0.90
	MetNav	0.04	0.35	0.99
Wind direction, °	NAM CONUS	4.46	12.26	0.65
	HRRR	−0.35	12.67	0.75
	GFS (0.25°)	3.43	13.33	0.71
	MetNav	−0.30	2.55	0.96
Temperature, °C	NAM CONUS	0.09	0.41	0.997
	HRRR	−0.10	0.41	0.997
	GFS (0.25°)	−1.74	1.84	0.997
	MetNav	−0.01	0.08	0.9998

* All comparisons are against MMS measurements (10 s averages, $n = 7749$). The Navigational Management System (MetNav) is a second, independent meteorological measurement suite on board the aircraft. Bias is the mean difference from MMS measurements. MAD is median absolute difference. R is the Pearson correlation coefficient.

3 Results

3.1 Meteorological dataset evaluation

Table 2 evaluates the accuracy of the three meteorological datasets used in this work against wind and temperature measurements (10 s averages) from the DC-8 aircraft. The evaluation focuses on periods and locations where the aircraft sampled smoke. In all three meteorological datasets, the mean biases are 0.25 $m\,s^{-1}$ or less for wind speed and 5° or less for wind direction. The median absolute differences are larger, but still 1.4 $m\,s^{-1}$ or less for wind speed and under 13° for wind direction. For comparison, two separate measurement systems on board the DC-8 (MMS and Navigational Management System) have median absolute differences of 0.34 $m\,s^{-1}$ in wind speed, 2.5° in wind direction. None of the meteorological datasets consistently outperformed the others across all wind performance metrics. For temperature, the high-resolution datasets (HRRR, NAM CONUS) have smaller mean and median errors than the lower-resolution GFS, but temperature is less relevant than wind for transport and smoke age calculations. In other circumstances, such as in the boundary layer or near frontal boundaries or convection, winds from the high-resolution models would likely perform better than GFS, but smoke plume sampling during FIREX-AQ primarily occurred in the lower free troposphere

and avoided severe weather. Based on their comparable overall wind representation, the trajectories computed with all three meteorological datasets are treated as an ensemble with equal weight for purposes of determining smoke age.

3.2 Smoke age evaluation: comparison of methods

This dataset provides age estimates every second for 24.3 h (87 370 s in 549 transects) of in situ smoke sampling by the DC-8 during FIREX-AQ and 18.9 h (68 157 s in 266 transects) of in situ smoke sampling by the Twin Otter. For the DC-8, this includes 20.1 h (302 transects) sampling smoke from 15 wildfires in the western US and 4.1 h (247 transects) sampling smoke from 89 prescribed, slash, and agricultural fires in the eastern US. These comprise nearly 97.5 % of in situ smoke samples by the DC-8. The remaining in situ smoke measurements did not have a clear source fire, so no age could be determined. Trajectory-based ages are provided for all of these smoke samples; mean-wind ages are provided for 323 crosswind and along-wind transects by the DC-8, where assumptions in the method are met. Smoke age estimates for the 10 fires sampled by the Twin Otter are solely from the trajectory-based method (see Sect. 2.3 for reasons). Table A1 summarizes the sampling dates and fires with smoke age estimates.

Figure 4 illustrates the difference between smoke ages from the mean-wind and trajectory-based methods using observations from the Shady Fire, Idaho, as an example. This fire was sampled by the NASA DC-8 on 25 July 2019 with 48 transects extending up to 160 km downwind of the fire. The mean-wind method produces a single age for each smoke transect, while the trajectory-based method allows the smoke age and its uncertainty to vary across each transect. For comparison between the methods, the trajectory-based ages are averaged across each transect and compared to the single mean-wind age for that transect. Age uncertainties (trajectory-based method only) are also averaged across each transect because the age errors in a single transect are expected to be highly correlated.

Overall, there is strong consistency between the age estimates from the mean-wind and trajectory-based methods for the Shady Fire. The two ages have strong linear correlation (Pearson $R = 0.95$) as well as rank correlation (Spearman $\rho = 0.97$). The mean relative difference between the two methods is 17 % for this fire, with the trajectory-based ages being older, which is comparable to the 20 % mean uncertainty in the trajectory-based ages for this day of sampling. Despite the overall consistency, however, the trajectory-based ages are systematically older than the mean-wind ages.

For smoke transects closest to the Shady Fire (< 40 km, age < 60 min; Fig. 4c), the two age estimates are within 10 min of each other, but the trajectory-based ages are systematically older than the mean-wind ages. For example, the two smoke transects closest to the Shady Fire had ages of 8 and 18 min according to the mean-wind method versus 16 ± 4 and 23 ± 4 min according to the trajectory-based method. The difference is almost entirely due to aging during buoyant plume rise, which is included in the trajectory-based age but not in the mean-wind age. The plume rise time for these transects close to the fire is about 6 min. If this plume rise time were added to the mean-wind age, the difference between the two methods would be less than 2 min, which is less than the uncertainty in the trajectory-based method. Thus, neglecting plume rise time in the mean-wind method is the cause of its systematic bias for young plumes. Users may, if desired, add the plume rise time from the trajectory method to the mean-wind age to mitigate this bias. In future applications, a plume rise component could be included in the mean-wind method.

At further distances (> 80 km, age > 100 min) additional differences between the two age methods appear. The oldest smoke, at the eastern end of sampling, is older according to the trajectory-based method than the mean-wind method by more than 1 h for some transects. The difference is primarily explained by the oldest samples being collected in the evening as winds slowed around sunset, a common meteorological phenomenon in the lower troposphere. The evening wind slowdown was recorded in the aircraft's wind measurements and visible in sequences of GOES images of the smoke plume, so it is a real effect that is represented in the trajectory-based age. Trajectories with high-resolution meteorology (HRRR, NAM CONUS) also suggest that the smoke plume ascended and descended by about 1 km when passing over mountains and valleys (Fig. 2). The mean-wind age, however, assumes constant winds at each altitude and that upwind transport occurred at the same altitude as the aircraft measurement. Future work could perhaps mitigate this limitation by computing the mean-wind age in a few segments where there are sufficient observations to characterize distinct wind regimes. An additional difference between the two age methods that can be seen in maps (Fig. 4a and b) is that the trajectory-based ages are older on the north side of the plume than the south side during some transects. The slower smoke transport on the north side of the plume also appears in GOES image sequences. Thus, the age differences in the far field smoke samples are due to temporal and horizontal wind shifts that are not accounted for in the mean-wind method.

Figure 5 compares the two age methods for a second example plume from the Sheridan Fire, Arizona. Terrain surrounding the Sheridan Fire has less topographic variation than the Shady Fire, which should make the winds more horizontally homogeneous and provide a better environment for the mean-wind age to perform well. Indeed, the two ages are very strongly correlated for the Sheridan Fire (Pearson $R = 0.99$). The mean-wind age is again systematically younger than the trajectory-based age for the first hour downwind of the fire, with the difference explained by the plume rise time (~ 5 min). After about one hour downwind, the trajectory-based ages are younger than the mean-wind ages,

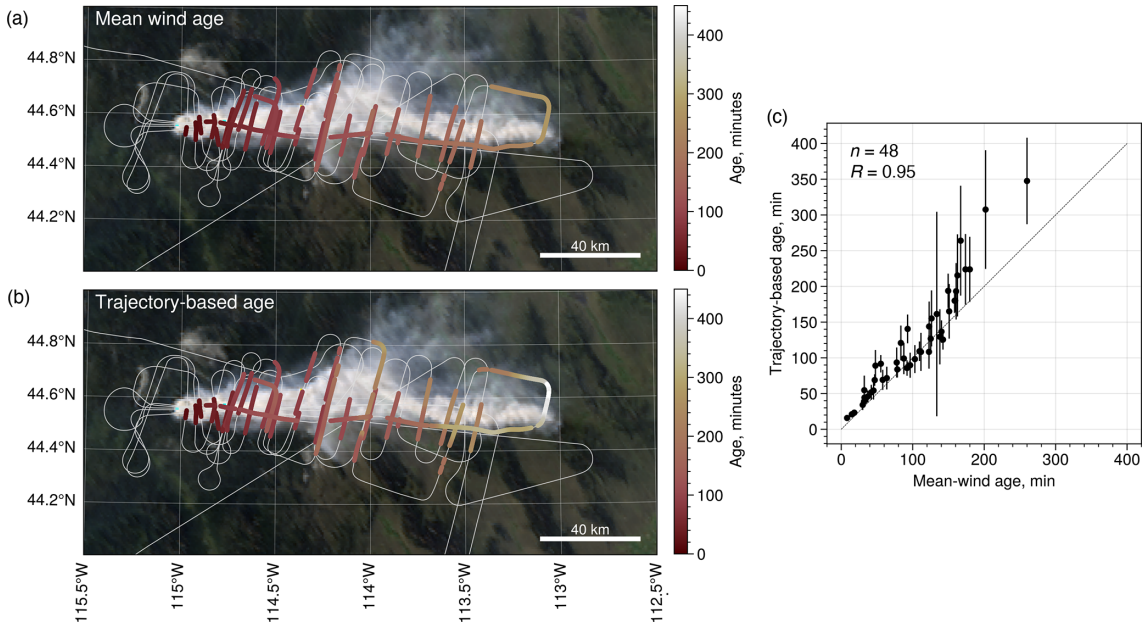


Figure 4. Smoke age for the Shady Fire, Idaho sampled by the NASA DC-8 on 25 July 2019, as determined by the mean-wind method **(a)**, trajectory-based method **(b)**, and comparison of the two methods **(c)**. Data in panels **(a)** and **(b)** are overlaid on true color imagery from GOES-East (26 July 2019 00:36 UTC). In panel **(c)**, each dot represents one transect and the diagonal gray line is 1 : 1. For the trajectory-based age, the mean age of the transect is shown, with a vertical line for the age uncertainty, while a single age is given for the entire transect in the mean-wind age.

as the meteorological datasets slightly overestimate the wind speed for this plume. The largest age differences between the two methods occur in the five most distant crosswind transects, which coincide with the plume passing over terrain on the edge of the Colorado Plateau in central Arizona. The high-resolution meteorological datasets have better capability to resolve winds around such topography, although their accuracy is not always guaranteed. The widths of these distant transects also increase to about 120 km, making the assumption of constant age across a transect less plausible. Evidence from Sheridan Fire and Shady Fire together supports that the two age methods having better agreement over flatter terrain.

Figure 6 expands the age comparison to all smoke plume transects sampled by the DC-8 during FIREX-AQ. There are 323 smoke plume transects with ages provided by both the mean-wind and trajectory-based methods, most of which (72 %) are in the western US. The mean-wind age could not be calculated for the Twin Otter, so the comparison in Fig. 6 only shows DC-8 data. The age comparison across all FIREX-AQ transects is similar to the results for the Shady plume already discussed. The linear correlation between the two methods is very strong (Pearson $R = 0.89$) and the mean relative difference is 12 %, with the trajectory-based ages being the older of the two. Plume rise accounts for about half of the mean difference between methods. At the youngest ages (< 60 min), we again see especially tight correlation between the two ages, with the trajectory-based age being systematically older because it accounts for aging during plume rise. The level of agreement between the two methods also reflects that the mean-wind method is not used for plumes with variable winds or beyond about 200 km, when age errors would likely be larger in this method.

3.3 Plume rise

The trajectory-based smoke ages here account for time elapsed during buoyant plume rise, as smoke ascends from the surface fire to its level of neutral buoyancy, after which plume transport becomes nearly horizontal. Figure 7 shows the distribution of plume rise heights for smoke sampled during FIREX-AQ, which are determined from the upwind trajectory altitudes where they pass over the fire (Sect. 2.4). For DC-8 observations, the mean smoke rise is 2500 m, with 95 % of the values in the range 300–5300 m. Many of the smallest rise heights occur over eastern US fires. The Twin Otter generally sampled smoke at lower altitudes than the DC-8 so the mean smoke rise is lower at 1700 m, with 95 % of the values being in the range 600–2700 m. The mean plume rise time is 5.7 min (95 % range: 0.7–12.2 min) for the DC-8 and 4.2 min (95 % range: 1.4–6.3 min) for the Twin Otter. Both the DC-8 and Twin Otter sampled smoke with less than 20 min of aging, so these observations, plume rise time is 30 %–50 % of the total age. Most smoke sampling was done farther downwind, however, so plume rise is less than 14 % of the smoke age for 95 % of the smoke measure-

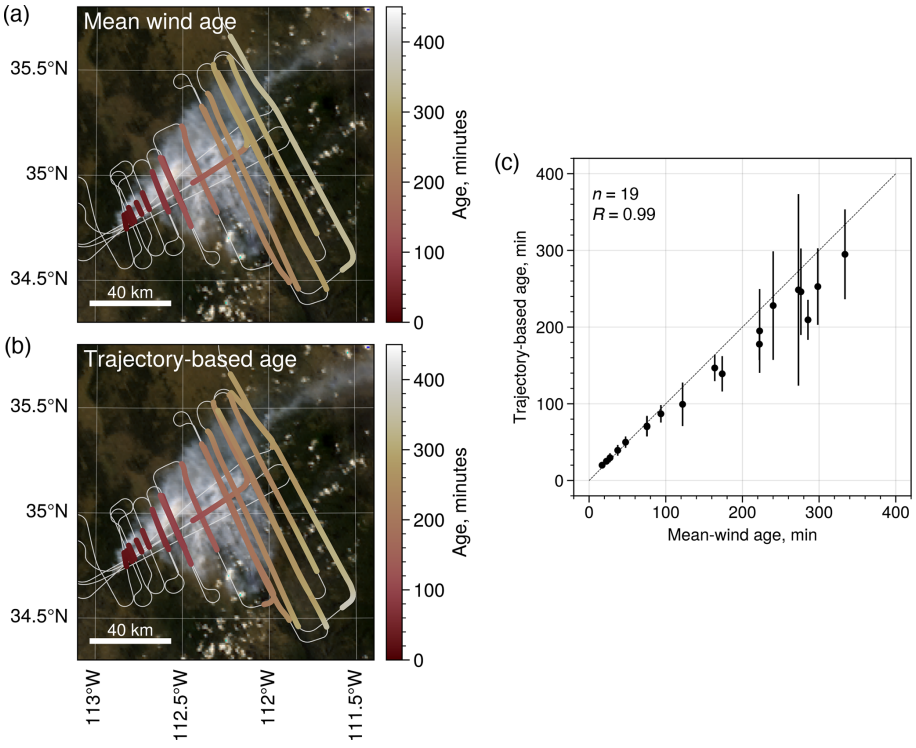


Figure 5. Smoke age for the Sheridan Fire, Arizona sampled by the NASA DC-8 on 16 August 2019, as determined by the mean-wind method **(a)**, trajectory-based method **(b)**, and comparison of the two methods **(c)**. Data in panels **(a)** and **(b)** are overlaid on true color imagery from GOES-East (17 August 2019 00:21 UTC). In panel **(c)**, each dot represents one transect and the diagonal gray line is 1 : 1. For the trajectory-based age, the mean age of the transect is shown, with a vertical line for the age uncertainty, while a single age is given for the entire transect in the mean-wind age.

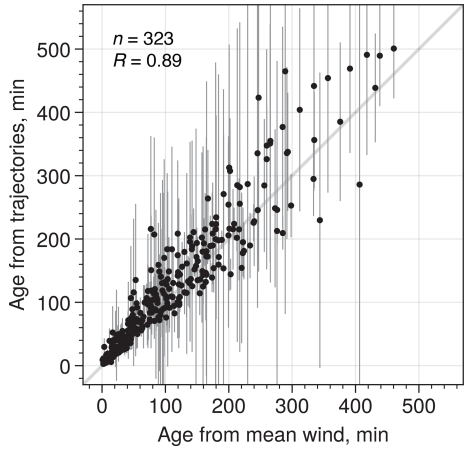


Figure 6. Comparison of smoke ages from the mean-wind and trajectory-based methods for all NASA DC-8 smoke transects with both age estimates during FIREX-AQ. Each dot represents one transect and the diagonal gray line is 1 : 1. For the trajectory-based age, the mean age of the transect is shown, with a vertical line for the age uncertainty, while a single age is given for the entire transect in the mean-wind age.

ments by the two aircraft. The mean fraction of smoke age coming from plume rise is 5 %. Thus, plume rise is small fraction of the age for most smoke samples collected during FIREX-AQ, but significant for accurate ages of the young smoke samples.

The plume rise contribution to smoke age is sensitive to the plume vertical speed, which is assumed to be $7 \pm 3.5\,\mathrm{m\,s^{-1}}$ in most plumes and $12 \pm 6\,\mathrm{m\,s^{-1}}$ in pyrocumulonimbus (Sect. 2.4). The limited literature on pyroconvective vertical velocities suggests that there is considerable variability in these speeds (Lareau and Clements, 2017; Rodriguez et al., 2020), which is the basis for the assumed 50 % relative uncertainty in vertical speed. The ensemble of meteorological models also provides a range of plume rise altitudes for each smoke observation, which is a second source of plume rise age uncertainty. However, mean uncertainty in plume rise height is 20 % of the height, so this has less impact on the results than uncertainty in rise speed. Uncertainty values are thus slightly greater than 50 % of the rise time, due to the rise speed being the dominant contributor to rise time uncertainty.

For 11 smoke plume transects ($n = 1443$ s) collected by the DC-8 in pyrocumulonimbus outflow (Peterson et al., 2022), the plume rise is about 3 times greater than the campaign average. For these samples, the mean plume rise is

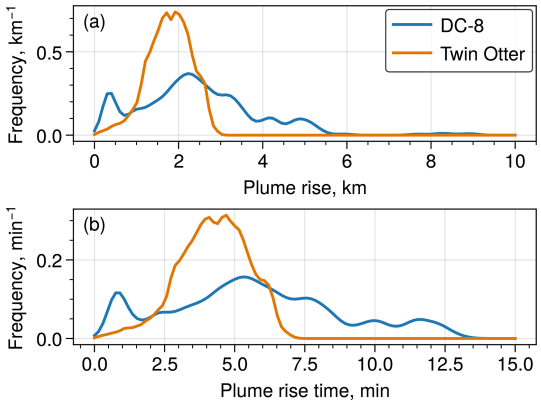


Figure 7. Distribution of plume rise heights **(a)** and plume rise times **(b)** for smoke measured during FIREX-AQ ($n = 87\,370$ s for the DC-8 and $n = 68\,157$ s for the Twin Otter). Plume rise heights are determined from the trajectories (Fig. 2, Sect. 2.4). All probability density functions are normalized to a unit integral.

7900 m (95 % range: 5800–9100 m) and these form a small, separate population in Fig. 7a. Despite the greater plume rise height, the plume rise time is within the range of other samples (Fig. 7b), because the vertical speed in pyrocumulonimbus convection is greater than the vertical speed in other pyroconvection (Sect. 2.4). The mean rise time for the pyrocumulonimbus is 11 min (95 % range: 8.1–12.6 min). Since the DC-8 measured pyrocumulonimbus outflow 19–170 min after it detrained at the cloud top, the plume rise comprises 13 % of the smoke age on average and up to 40 % of the smoke age for some samples.

3.4 Smoke age uncertainty

The dataset presented here provides two ways of assessing the uncertainty in smoke age, both of which are shown in Fig. 8. The trajectory-based age method internally quantifies the uncertainty in each smoke age value. From this method, the median smoke age uncertainty is 23 % of the smoke age for DC-8 observations and 16 % for Twin Otter observations. The leading factor contributing to this uncertainty is the spread in upwind advection ages in the ensemble of meteorological datasets (term 1 in Sect. 2.4, Fig. 8). This age uncertainty from the advection ensemble alone is 13 %–15 % of smoke age for both the DC-8 and Twin Otter observations. The second-largest factor contributing to age uncertainty is wind speed errors in the meteorological datasets (term 4), which contributes 11 % uncertainty for the DC-8 smoke ages and could not be assessed for the Twin Otter. Plume rise and other terms in the trajectory-based age analysis contribute much less to smoke age uncertainty for both aircraft (≤ 5 %). An additional uncertainty for pyrocumulonimbus smoke is that, after detrainment from the deep convective column, unresolved vertical winds within and around the active anvil cloud could transport smoke vertically, which is not included in the trajectories. For the specific pyrocumulonimbus over the Williams Flats fire, the effect magnitude is bounded by the measured horizontal wind speed in the active anvil ($\sim 12\,\mathrm{m\,s^{-1}}$), range in wind speed from the anvil top to bottom altitudes (~ 30 %), and horizontal extent of the active anvil (~ 50 km), which gives an upper bound age uncertainty of ~ 20 min (~ 20 % of mean smoke age in these transects) due to unresolved vertical transport within the anvil. Figure 8 compares the age uncertainty components for the DC-8 and Twin Otter, showing that they are similar except for the wind speed term that could only be estimated for the DC-8. The lack of a wind speed uncertainty term for the Twin Otter therefore likely explains the apparently higher median total uncertainty for the DC-8 (24 % vs. 16 %). The larger mean and median uncertainty statistics for the DC-8, therefore, should be considered representative for both aircraft during FIREX-AQ.

Comparison between the mean-wind and trajectory-based ages provides a second way of assessing smoke age uncertainty. This comparison is only possible for the subset of DC-8 smoke observations in which the mean-wind method provides an age estimate. The median absolute difference between the two methods is 15 % and the mean is slightly larger at 21 %. As reported in Sect. 3.2, the mean-wind age is systematically 12 % younger than the trajectory-based age on average. Thus, the absolute differences between the two age methods are mainly systematic, not random. The slightly lower median uncertainty suggested by the comparison between two age methods may be because the mean-wind method was not used in cases with long-range transport or shifting winds, where ages may be inherently more uncertain. Moreover, the trajectory-based method provides an uncertainty for each age estimate. In applications that derive chemical rates from samples spanning a range of plume ages, age uncertainties translate directly to uncertainties in inferred rates or timescales. For a first-order process (e.g. exponential growth or decay), a ~ 20 % age uncertainty implies a similar relative uncertainty in the fitted rate, though combining multiple observations reduces this when age errors are not strongly correlated. In addition, these uncertainty values can inform measurement interpretation by identifying periods with higher or lower confidence in smoke age or by applying uncertainty-based weighting in statistical models of smoke evolution.

4 Data availability

The data described and used in this paper are contained in the NASA-NOAA FIREX-AQ data archive, which is housed at the NASA Atmospheric Science Data Center (ASDC): https://doi.org/10.5067/SUBORBITAL/FIREXAQ2019/DATA001 (FIREX-AQ Science Team, 2019). The specific data products used in this work are:

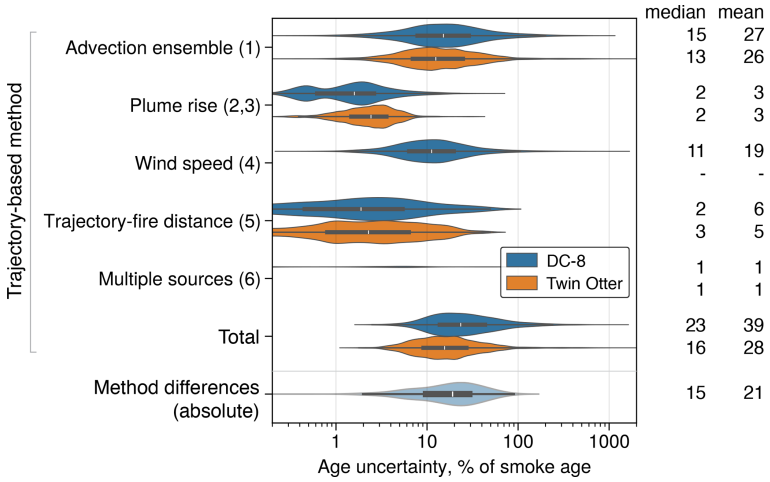


Figure 8. Distribution of smoke age uncertainty and factors contributing to the uncertainty during FIREX-AQ. The width of each violin shape represents the relative frequency of data values ($n = 87{,}370$ s for DC-8 and $n = 68{,}157$ s for Twin Otter); black bars and white dots within each violin show the interquartile range and median, respectively. Parenthetical numbers in the left axis group labels specify the uncertainty components listed in Sect. 2.4. The median and mean of each distribution are provided by the right axis.

- Tabular data summary of each NASA DC-8 smoke transect associating it with the source fire name, location, and fuel: https://doi.org/10.5067/ASDC/FIREXAQ_Analysis_Data_1 (Gargulinski et al., 2021). See the file prefix FIREXAQ-FIREFLAG-TABULARDATA.

- Smoke age and meteorological measurements for the NASA DC-8: https://doi.org/10.5067/ASDC/FIREXAQ_MetNav_AircraftInSitu_DC8_Data_1 (Bennett et al., 2020). Files with the prefix firexaq-fire-Flags contain mean-wind ages; files with the prefix FIREXAQ-FSU-SMOKEAGE contain trajectory-based ages; files with the prefix FIREXAQ-MMS contain meteorological data and aircraft location coordinates.

- Smoke age (trajectory-based method) for the NOAA Chemistry Twin Otter: https://doi.org/10.5067/ASDC/SUBORBITAL/FIREXAQ_Analysis_N48_Data_1 (Holmes, 2021a).

- GOES ABI true-color imagery: https://doi.org/10.5067/ASDC/FIREXAQ_Satellite_Data_2 (Holmes, 2021b). Files with the prefix FIREXAQ-GOES*nn*-IMAGES, where the satellite number *nn* is 16 or 17, contain still images (png) and animations (mp4). Files with the prefix FIREXAQ-GOES*nn*-DATA contain data (netCDF4 format) used to create the images.

Key smoke age variables from both the mean-wind and trajectory-based methods (age, plume rise, uncertainty) are also contained in aircraft "merge" files that combine measurements from multiple instruments into a single file for each flight (https://doi.org/10.5067/ASDC/FIREXAQ_MERGE_DATA_2, Crawford et al., 2022). Many of these data files use the ICARTT file format (Northup et al., 2017). Software tools are available to read ICARTT files in Python (e.g. Knote, 2022) and other languages (https://www-air.larc.nasa.gov/tools.htm, last access: 15 August 2026).

The HYSPLIT model is available from https://www.ready.noaa.gov/HYSPLIT.php (last access: 7 July 2023). Meteorology data for HYSPLIT (GFS, NAM CONUS, HRRR) are available from https://www.ready.noaa.gov/data/archives/ (last access: 15 August 2026).

5 Conclusions

Two methods for determining smoke age have been applied to in situ aircraft observations from the NASA-NOAA FIREX-AQ field campaign. The mean-wind method infers the age from the mean vertical profile of measured winds near the fire and the downwind distance from the fire to the observation point. The trajectory-based method uses an ensemble of upwind trajectories from the observation location, accounts for plume rise time, and provides an internal uncertainty estimate. Both methods are applied to DC-8 observations, and the trajectory-based method is applied to smoke observed by the NOAA Chemistry Twin Otter. In total, the dataset includes smoke age estimates for 24.3 h (549 transects) observing smoke in situ from 104 fires by the DC-8 and nearly 19 h (266 transects) observing smoke from 10 fires by the Twin Otter. The large scope, treatment of plume

rise, and thorough uncertainty quantification are novel aspects of this smoke age dataset.

This work also describes true color imagery and movies created from the ABI instrument on GOES-East and GOES-West satellites. The satellite imagery includes a terrain parallax correction, so that surface features appear at the correct latitude and longitude. For fires in mountainous western US, the parallax correction shifts the apparent locations by 2–8 km. As a result, smoke plumes in the terrain-corrected images appear over the true fire locations, rather than appearing displaced from the fires by many kilometers. Satellite imagery is used to exclude upwind trajectories from the trajectory-based age analysis when a meteorological dataset shows large inconsistencies in wind direction or speed relative to the observed smoke plume transport. The age estimate is then based on the remaining trajectories that are consistent with the actual plume transport.

The main strength of the mean-wind method is that it does not depend on the availability or accuracy of meteorological analysis datasets. Therefore, the mean-wind method is best suited for short-range transport under steady wind conditions with minimal terrain effects on the wind. Indeed, the mean-wind method was not used during FIREX-AQ for cases of long-range plume transport or days with especially variable winds. The strengths of the trajectory-based method are that it includes plume rise, accounts for spatial and temporal wind variation, works when wind measurements are not available (e.g. Twin Otter), and provides an uncertainty estimate. The trajectory-based age method is sensitive to errors in meteorological datasets. While the three meteorological datasets used (HRRR, NAM CONUS, GFS) here have small mean biases in wind speed ($< 0.25\,\mathrm{m\,s^{-1}}$) and wind direction ($< 5\,^{\circ}$) during FIREX-AQ smoke sampling, errors are sometimes larger. In the trajectory-based method, the difference between measured and modeled wind speed informs the age uncertainty estimate, so the user can identify intermittent periods of greater age uncertainty.

Age estimates from the two methods can be compared for 323 smoke plume transects collected by the DC-8 during FIREX-AQ. While the two ages are strongly correlated ($R = 0.89$), the mean-wind age is 12 % younger than the trajectory-based age on average. This systematic difference is most noticeable for young smoke observations (< 60 min) due to the buoyant plume rise time being included in the trajectory-based age but not in the mean-wind age. Plume rise accounts for about half of mean relative difference between the age methods. In future applications, plume rise could be incorporated into the mean-wind method. Some of the older smoke observations (> 100 min) were collected in the evening as wind speeds in the boundary layer decayed. By assuming constant wind speeds, the mean-wind method underestimates the age of these evening smoke samples, while the meteorological datasets and trajectory-based age have the capability to resolve these wind changes.

The uncertainty in smoke age can be obtained from the trajectory-based method, which provides the uncertainty for each age value. The median age uncertainty for FIREX-AQ smoke observations is 24 % of the smoke age. The distribution of uncertainty values has a long tail, however, so the mean age uncertainty is larger 37 %. The level of accuracy required of age data depends on the application. In analyses that quantify chemical transformations, age uncertainty limits how tightly rates can be constrained, although this limitation diminishes when multiple observations with largely independent errors are combined. The age uncertainties can also guide data interpretation by identifying periods with high and low confidence in the age or by providing weight factors for statistical models of smoke evolution. The main source of age uncertainty is ensemble spread between the three meteorological models used to compute trajectories (13 %–15 %) and the second-largest source of uncertainty is due to disagreement between measured and modeled wind speed (~ 11 %). Other factors, like plume rise and ambiguity in the source fire contribute much less to age uncertainty during FIREX-AQ (< 5 %).

The smoke age products described here provide a basis for interpreting measurements of chemical and physical aging in the smoke observations during FIREX-AQ. These enabled analyses have been applied to composition and optical properties of aerosols (Adachi et al., 2024; Azzarello et al., 2023; Pagonis et al., 2023; Saide et al., 2022; Washenfelder et al., 2022) and trace gases (Decker et al., 2021a, b, 2024; Robinson et al., 2021; Xu et al., 2021). Plume rise time is a significant fraction of the smoke age for measurements near the fire source, so it should be considered when interpreting measurements or comparing to models. The techniques for inferring aging during plume rise, using satellite data to screen implausible trajectories from ensembles, and assessing uncertainty in the trajectory-based ages may be useful for other applications where age estimates are needed, including other studies of smoke and long-range plume transport more generally.

Appendix A

Table A1. Summary of smoke ages sampled during FIREX-AQ.

Aircraft	Flight Date	Fire Name[a]	Fire ID[b]	State	Fuel	Transects[c]		Trajectory-based age (minutes)		Mean-wind age[d] (minutes)	
						n	types	mean	range	mean	range
DC-8	24 Jul 2019	Sheep	0	ID	shrubland	7	o	37	3–73	–	–
DC-8	24 Jul 2019	Shady	1	ID	understory	3	c	29	12–49	25	12–36
DC-8	25 Jul 2019	Shady	1	ID	understory	47	cao	156	16–495	121	8–272
DC-8	29 Jul 2019	North Hills	3	MT	savanna	13	c	111	9–604	116	5–246
DC-8	29 Jul 2019	Tucker	4	CA	shrubland	12	ca	152	26–526	121	21–292
DC-8	30 Jul 2019	Tucker	4.1	CA	shrubland	2	o	1207	883–2465	–	–
DC-8	30 Jul 2019	Lefthand	5	WA	forest	12	co	441	258–641	350	192–460
DC-8	2 Aug 2019	Ridgetop	6	MT	grassland	6	o	70	10–154	–	–
DC-8	2 Aug 2019	Lick Creek	7	ID	forest	12	c	122	24–212	130	23–234
DC-8	3 Aug 2019	Williams Flats	10	WA	grassland	34	co	201	11–810	170	7–406
DC-8	6 Aug 2019	Williams Flats	10	WA	forest	9	cao	104	8–214	105	5–259
DC-8	6 Aug 2019	Williams Flats	10.1	WA	forest	1	o	1068	401–1539	–	–
DC-8	6 Aug 2019	Williams Flats	10.2	WA	forest	1	o	382	165–560	–	–
DC-8	6 Aug 2019	Horsefly	11	MT	forest	14	co	146	62–219	119	47–201
DC-8	7 Aug 2019	Williams Flats	10	WA	forest	21	co	514	35–2409	122	32–239
DC-8	8 Aug 2019	Williams Flats	10	WA	forest	11	o	1042	30–2004	–	–
DC-8	8 Aug 2019	Williams Flats	10.3	WA	forest	2	o	1181	685–1758	–	–
DC-8	12 Aug 2019	Castle	12	AZ	forest	20	ca	237	23–536	203	22–431
DC-8	13 Aug 2019	Castle	12	AZ	forest	21	c	202	25–934	147	19–260
DC-8	13 Aug 2019	Ikes	12.1	AZ	understory	2	c	53	31–77	34	17–50
DC-8	15 Aug 2019	Castle	12	AZ	forest	1	o	503	147–1018	–	–
DC-8	15 Aug 2019	Trumbull	12.5	AZ	forest	1	o	444	247–884	–	–
DC-8	15 Aug 2019	Sheridan	13	AZ	forest	15	o	162	8–926	–	–
DC-8	15 Aug 2019	Saber	13.1	AZ	understory	1	o	77	62–97	–	–
DC-8	15 Aug 2019	Boulin	13.2	AZ	forest	2	o	76	45–97	–	–
DC-8	15 Aug 2019	Sheridan	13.3	AZ	forest	1	o	776	702–1279	–	–
DC-8	16 Aug 2019	Sheridan	13	AZ	forest	21	cao	208	16–379	235	17–334
DC-8	21 Aug 2019	–	14	TX	savanna	1	a	30	27–36	39	31–47
DC-8	21 Aug 2019	–	14.1	TX	forest	1	c	30	9–58	4	–
DC-8	21 Aug 2019	–	15	TX	slash	5	o	136	2–423	–	–
DC-8	21 Aug 2019	–	15.5	TX	pile	1	o	15	2–30	–	–
DC-8	21 Aug 2019	–	16	LA	cropland	4	o	50	3–125	–	–
DC-8	21 Aug 2019	–	17	LA	cropland	4	o	48	3–133	–	–
DC-8	21 Aug 2019	–	18	LA	structure/ urban	2	o	6	3–12	–	–
DC-8	21 Aug 2019	–	19	LA	cropland	3	o	9	3–21	–	–
DC-8	21 Aug 2019	–	20	LA	cropland	2	o	35	3–166	–	–
DC-8	21 Aug 2019	–	21	MS	cropland	1	o	4	2–6	–	–
DC-8	21 Aug 2019	–	21.1	MS	cropland	1	o	13	3–27	–	–
DC-8	21 Aug 2019	–	22	MS	cropland	2	o	33	3–95	–	–
DC-8	21 Aug 2019	–	23	MS	cropland	2	o	9	5–18	–	–
DC-8	23 Aug 2019	–	24	MS	cropland	2	o	14	3–28	–	–
DC-8	23 Aug 2019	–	25	MS	cropland	3	o	11	5–22	–	–
DC-8	23 Aug 2019	–	26	MS	cropland	7	o	30	3–95	–	–
DC-8	23 Aug 2019	–	27	MS	pile	1	o	22	4–41	17	–
DC-8	23 Aug 2019	–	28	MS	cropland	5	o	45	10–96	–	–
DC-8	23 Aug 2019	–	29	LA	cropland	2	o	10	3–25	–	–
DC-8	23 Aug 2019	–	30	LA	shrubland	2	o	59	4–148	–	–
DC-8	23 Aug 2019	–	31	LA	cropland	6	o	46	3–116	–	–
DC-8	23 Aug 2019	–	32	LA	cropland	2	o	8	2–20	–	–
DC-8	23 Aug 2019	–	33	LA	cropland	2	o	5	2–9	–	–
DC-8	23 Aug 2019	–	34	AR	cropland	1	o	368	104–931	–	–
DC-8	23 Aug 2019	–	35	MS	cropland	4	o	85	6–191	–	–

Table A1. Continued

Aircraft	Flight Date	Fire Name[a]	Fire ID[b]	State	Fuel	Transects[c]		Trajectory-based age (minutes)		Mean-wind age[d] (minutes)	
						n	types	mean	range	mean	range
DC-8	23 Aug 2019	–	36	MS	cropland	2	o	87	26–140	–	–
DC-8	26 Aug 2019	–	37	OK	slash	10	cao	37	1–92	39	1–84
DC-8	26 Aug 2019	–	38	AR	slash	2	co	39	2–97	20	20–20
DC-8	26 Aug 2019	–	39	TX	cropland	3	cao	19	2–44	25	3–55
DC-8	26 Aug 2019	–	40	LA	cropland	4	o	16	2–30	–	–
DC-8	26 Aug 2019	–	41	LA	cropland	2	o	8	2–14	–	–
DC-8	26 Aug 2019	–	42	LA	cropland	1	o	12	4–22	–	–
DC-8	26 Aug 2019	–	43	LA	cropland	6	cao	74	2–186	96	44–172
DC-8	26 Aug 2019	–	44	LA	cropland	5	ca	79	2–188	97	1–183
DC-8	26 Aug 2019	–	45	OK	forest	5	cao	14	2–31	17	3–43
DC-8	26 Aug 2019	–	45.1	OK	slash	1	o	50	48–53	–	–
DC-8	29 Aug 2019	Hickory Ridge WMA	46	NE	grassland	7	ca	29	3–68	25	0–60
DC-8	29 Aug 2019	Tallgrass Prairie Preserve	47	KS	grassland	7	ca	24	2–53	25	0–60
DC-8	29 Aug 2019	–	48	KS	pile	3	o	7	5–10	–	–
DC-8	29 Aug 2019	–	49	KS	cropland	1	o	2	1–3	–	–
DC-8	29 Aug 2019	–	49.5	KS	cropland	1	o	4	4–4	–	–
DC-8	29 Aug 2019	–	50	OK	grassland	1	a	11	2–20	9	1–19
DC-8	29 Aug 2019	–	50.5	OK	grassland	1	o	26	18–40	–	–
DC-8	29 Aug 2019	–	51	KS	grassland	1	a	57	3–109	57	1–117
DC-8	30 Aug 2019	Blackwater River SF	52	FL	understory	21	ca	80	4–200	58	1–160
DC-8	30 Aug 2019	–	53	GA	shrubland	1	o	13	9–18	–	–
DC-8	30 Aug 2019	–	54	GA	pile	2	o	14	1–28	–	–
DC-8	30 Aug 2019	–	55	GA	slash	1	o	8	1–16	–	–
DC-8	30 Aug 2019	–	56	GA	slash	1	o	11	2–19	–	–
DC-8	30 Aug 2019	–	57	GA	cropland	3	o	15	2–33	–	–
DC-8	30 Aug 2019	–	58	GA	cropland	1	a	101	67–140	–	–
DC-8	30 Aug 2019	–	59	GA	pile	2	o	6	2–12	–	–
DC-8	30 Aug 2019	–	60	GA	cropland	1	o	148	142–162	–	–
DC-8	30 Aug 2019	–	61	GA	cropland	1	a	30	2–54	29	4–58
DC-8	30 Aug 2019	–	62	AL	slash	3	ca	21	2–52	24	3–62
DC-8	30 Aug 2019	–	63	AL	slash	1	o	19	4–32	–	–
DC-8	30 Aug 2019	–	64	AL	slash	5	ao	132	3–312	89	5–170
DC-8	31 Aug 2019	–	65	MS	cropland	3	ao	35	5–83	34	9–63
DC-8	31 Aug 2019	–	66	MS	cropland	1	a	72	13–154	41	1–83
DC-8	31 Aug 2019	–	67	MS	cropland	1	o	11	1–24	–	–
DC-8	31 Aug 2019	–	68	MS	cropland	2	o	5	2–9	–	–
DC-8	31 Aug 2019	–	69	MS	cropland	4	ao	21	1–53	22	7–45
DC-8	31 Aug 2019	–	70	MS	cropland	1	o	10	5–15	–	–
DC-8	31 Aug 2019	–	70.1	AR	cropland	1	o	5	4–5	–	–
DC-8	31 Aug 2019	–	71	AR	cropland	6	ao	61	3–166	23	7–50
DC-8	31 Aug 2019	–	72	AR	cropland	2	o	26	2–94	–	–
DC-8	31 Aug 2019	–	73	MS	cropland	2	o	7	5–11	–	–
DC-8	31 Aug 2019	–	74	MS	cropland	2	ao	34	1–80	34	10–62
DC-8	31 Aug 2019	–	75	MS	cropland	4	ao	13	2–36	17	6–42
DC-8	31 Aug 2019	–	76	MS	cropland	3	ao	5	1–12	11	5–24
DC-8	31 Aug 2019	–	77	MS	cropland	2	o	19	4–37	–	–
DC-8	31 Aug 2019	–	78	LA	slash	8	ao	32	3–75	–	–
DC-8	3 Sep 2019	–	80	MO	cropland	3	ca	62	3–169	82	1–210
DC-8	3 Sep 2019	–	81	MO	shrubland	1	o	8	5–10	–	–
DC-8	3 Sep 2019	–	82	IL	cropland	2	ca	17	3–35	20	1–46
DC-8	3 Sep 2019	–	83	AR	cropland	1	o	15	5–25	–	–
DC-8	3 Sep 2019	–	84	AR	cropland	2	o	57	6–130	–	–

Table A1. Continued

Aircraft	Flight Date	Fire Name[a]	Fire ID[b]	State	Fuel	Transects[c]		Trajectory-based age (minutes)		Mean-wind age[d] (minutes)	
						n	types	mean	range	mean	range
DC-8	3 Sep 2019	–	85	AR	cropland	3	ao	43	4–88	22	4–47
DC-8	3 Sep 2019	–	86	AR	pile	1	o	25	3–67	–	–
DC-8	3 Sep 2019	–	87	AR	cropland	1	o	15	5–28	–	–
DC-8	3 Sep 2019	–	88	AR	pile	1	o	99	5–210	–	–
DC-8	3 Sep 2019	–	89	AR	cropland	4	o	68	7–192	–	–
DC-8	3 Sep 2019	–	90	AR	cropland	4	cao	47	3–116	30	4–64
DC-8	3 Sep 2019	–	91	AR	cropland	2	ca	46	1–101	51	9–64
DC-8	3 Sep 2019	–	92	MS	cropland	1	o	7	3–12	–	–
DC-8	3 Sep 2019	–	93	MS	cropland	1	o	5	3–7	–	–
DC-8	3 Sep 2019	–	93.1	MS	cropland	1	o	8	4–12	–	–
DC-8	3 Sep 2019	–	93.2	MS	cropland	1	o	8	3–18	–	–
DC-8	3 Sep 2019	–	94	MS	cropland	1	o	13	3–26	–	–
Twin Otter	29 Jul 2019	–	1	CO	cropland	2	–	5	4–7	–	–
Twin Otter	5 Aug 2019	Goose	2	NV	shrubland	5	–	99	34–467	–	–
Twin Otter	9 Aug 2019	HK163	3	OR	forest	11	–	112	61–203	–	–
Twin Otter	9 Aug 2019	Nethker	4	ID	forest	6	–	68	39–106	–	–
Twin Otter	16 Aug 2019	Granite Gulch	5	OR	forest	25	–	65	6–121	–	–
Twin Otter	17 Aug 2019	Granite Gulch	5	OR	forest	13	–	66	42–111	–	–
Twin Otter	20 Aug 2019	Little Bear	7	UT	forest	13	–	141	4–225	–	–
Twin Otter	20 Aug 2019	Ikes	11	AZ	forest	10	–	267	93–699	–	–
Twin Otter	21 Aug 2019	Castle	6	AZ	forest	4	–	18	3–35	–	–
Twin Otter	21 Aug 2019	Little Bear	7	UT	forest	12	–	51	16–104	–	–
Twin Otter	21 Aug 2019	Ikes	11	AZ	forest	9	–	293	110–420	–	–
Twin Otter	24 Aug 2019	204 Cow	8	OR	forest	38	–	119	30–244	–	–
Twin Otter	25 Aug 2019	204 Cow	8	OR	forest	22	–	122	26–217	–	–
Twin Otter	27 Aug 2019	204 Cow	8	OR	forest	23	–	370	76–1048	–	–
Twin Otter	28 Aug 2019	204 Cow	8	OR	forest	24	–	170	39–836	–	–
Twin Otter	3 Sep 2019	204 Cow	8	OR	forest	22	–	101	36–366	–	–
Twin Otter	4 Sep 2019	204 Cow	8	OR	forest	1	–	101	92–111	–	–
Twin Otter	4 Sep 2019	Canyon 66	9	OR	forest	19	–	107	45–194	–	–
Twin Otter	5 Sep 2019	Smith Knob	10	ID	forest	7	–	213	14–445	–	–

[a] Wildfire names are from incident reports (National Interagency Coordination Center, 2019). Prescribed fires are unnamed, except three fires in FL, KS and NE that are named by their land management organizations. WMA = Wildlife Management Area, SF = State Forest. [b] Fire ID numbers used across FIREX-AQ datasets and defined in the TABULARDATA file described in Sect. 4 for the DC-8 (Gargulinski et al., 2021). The TABULARDATA file also identifies fires and transects for which no smoke ages are computed. [c] Number of transects (*n*) and transect types. Transect types are c = crosswind (i.e. transverse), a = along wind (i.e. longitudinal), o = other or unknown; multiple letters indicate multiple transect types (e.g. ca means both crosswind and along wind transects were sampled). Mean-wind ages are not calculated for other type transects. No type was assigned for Twin Otter transects since the mean-wind method was not used. [d] The mean and range of ages for the mean-wind method is based on crosswind and along-wind transects (types c and a), while the mean and range for the trajectory-based method include all transect types (c, a and o).

Author contributions. CDH and JPS conceived the research goals, performed data analysis, and curated data. CDH, JPS, and RY formulated the smoke age methods with input from DAP. CDH, CHF, HKN, and AA developed software. RAW, MAR, ZCJD, KB, EMG, AJS, TPB, JD, SK, CX, JPD, JBN, HH and GSD provided data used in the analysis. CDH prepared the manuscript with contributions from all co-authors.

Competing interests. The contact author has declared that none of the authors has any competing interests.

Disclaimer. Views expressed are those of authors and do not reflect those of NOAA or the US Department of Commerce.

Publisher's note: Copernicus Publications remains neutral with regard to jurisdictional claims made in the text, published maps, institutional affiliations, or any other geographical representation in this paper. The authors bear the ultimate responsibility for providing appropriate place names. Views expressed in the text are those of the authors and do not necessarily reflect the views of the publisher.

Acknowledgements. This work was supported by NASA grants 80NSSC18K0625 (CDH), 80NSSC19K1368 (CDH, CHF), 80HQTR18T0063 (DAP), 80HQTR21T0099 (DAP), NNX14AP45G (RJY), 80NSSC21K1456 (AJS, EMG), NSF-AGS grant 1748266 (RJY), NOAA grant NA16OAR4310100 (RJY), and the NOAA AC4 program (JPS). We acknowledge the use of data and/or imagery from NASA's Fire Information for Resource Management System (FIRMS) (https://www.earthdata.nasa.gov/data/tools/firms, last access: 7 July 2023), part of NASA's Earth Science Data and Information System (ESDIS).

Financial support. This research has been supported by the National Aeronautics and Space Administration (grant nos. 80NSSC18K0625, 80NSSC19K1368, 80NSSC21K1456, 80HQTR18T0063, 80HQTR21T0099, and NNX14AP45G), the National Science Foundation (grant no. 1748266), and the National Oceanic and Atmospheric Administration (grant no. NA16OAR4310100).

Review statement. This paper was edited by Fan Mei and reviewed by four anonymous referees.

References

Adachi, K., Dibb, J. E., Katich, J. M., Schwarz, J. P., Guo, H., Campuzano-Jost, P., Jimenez, J. L., Peischl, J., Holmes, C. D., and Crawford, J.: Occurrence, abundance, and formation of atmospheric tarballs from a wide range of wildfires in the western US, Atmos. Chem. Phys., 24, 10985–11004, https://doi.org/10.5194/acp-24-10985-2024, 2024.

Akagi, S. K., Craven, J. S., Taylor, J. W., McMeeking, G. R., Yokelson, R. J., Burling, I. R., Urbanski, S. P., Wold, C. E., Seinfeld, J. H., Coe, H., Alvarado, M. J., and Weise, D. R.: Evolution of trace gases and particles emitted by a chaparral fire in California, Atmos. Chem. Phys., 12, 1397–1421, https://doi.org/10.5194/acp-12-1397-2012, 2012.

Azzarello, L., Washenfelder, R. A., Robinson, M. A., Franchin, A., Womack, C. C., Holmes, C. D., Brown, S. S., Middlebrook, A., Newberger , T., Sweeney , C., and Young, C. J.: Characterization of water-soluble brown carbon chromophores from wildfire plumes in the western USA using size-exclusion chromatography, Atmos. Chem. Phys., 23, 15643–15654, https://doi.org/10.5194/acp-23-15643-2023, 2023.

Bah, M. K., Gunshor, M. M., and Schmit, T. J.: Generation of GOES-16 True Color Imagery without a Green Band, Earth Space Sci., 5, 549–558, https://doi.org/10.1029/2018EA000379, 2018.

Bennett, J. R., Bui, T. P., Dean-Day, J., Diskin, G. S., Drdla, K., Gargulinski, E., Holmes, C. D., Peischl, J., Ryerson, T., Schwarz, J. P., Soja, A., Wiggins, E., and Yang Martin, M.: FIREX-AQ DC8 In-Situ Meteorological and Navigational Data, NASA [data set], https://doi.org/10.5067/ASDC/FIREXAQ_METNAV_AIRCRAFTINSITU_DC8_DATA_1, 2020.

Briggs, G. A.: Plume Rise: A Critical Survey, TID-25075, U.S. Atomic Energy Commission, Oak Ridge, Tennessee, https://doi.org/10.2172/4743102, 1969.

Clements, C. B., Lareau, N. P., Kingsmill, D. E., Bowers, C. L., Camacho, C. P., Bagley, R., and Davis, B.: The Rapid Deployments to Wildfires Experiment (RaDFIRE): Observations from the Fire Zone, B. Am. Meteorol. Soc., 99, 2539–2559, https://doi.org/10.1175/BAMS-D-17-0230.1, 2018.

Crawford, J., Al-Saadi, J., Dibb, J., Frost, G., Kalshnikova, O. V., Lefer, B., Schwarz, J. P., Seidel, F., Warneke, C., Ahren, A., Apel, E., Blake, D., Bui, T. P., Diskin, G. S., Fried, A., Gilman, J., Hall, S., Hanisco, T., Hannun, R., …, and Yang Martin, M.: FIREX-AQ Merge Data Files [Dataset], NASA Langley Atmospheric Science Data Center Distributed Active Archive Center [data set], https://doi.org/10.5067/ASDC/FIREXAQ_MERGE_DATA_2, 2022.

Crosson, E. R.: A cavity ring-down analyzer for measuring atmospheric levels of methane, carbon dioxide, and water vapor, Appl. Phys. B, 92, 403–408, https://doi.org/10.1007/s00340-008-3135-y, 2008.

Decker, Z. C. J., Robinson, M. A., Barsanti, K. C., Bourgeois, I., Coggon, M. M., DiGangi, J. P., Diskin, G. S., Flocke, F. M., Franchin, A., Fredrickson, C. D., Gkatzelis, G. I., Hall, S. R., Halliday, H., Holmes, C. D., Huey, L. G., Lee, Y. R., Lindaas, J., Middlebrook, A. M., Montzka, D. D., Moore, R., Neuman, J. A., Nowak, J. B., Palm, B. B., Peischl, J., Piel, F., Rickly, P. S., Rollins, A. W., Ryerson, T. B., Schwantes, R. H., Sekimoto, K.,

Thornhill, L., Thornton, J. A., Tyndall, G. S., Ullmann, K., Van Rooy, P., Veres, P. R., Warneke, C., Washenfelder, R. A., Weinheimer, A. J., Wiggins, E., Winstead, E., Wisthaler, A., Womack, C., and Brown, S. S.: Nighttime and daytime dark oxidation chemistry in wildfire plumes: an observation and model analysis of FIREX-AQ aircraft data, Atmos. Chem. Phys., 21, 16293–16317, https://doi.org/10.5194/acp-21-16293-2021, 2021a.

Decker, Z. C. J., Wang, S., Bourgeois, I., Campuzano Jost, P., Coggon, M. M., DiGangi, J. P., Diskin, G. S., Flocke, F. M., Franchin, A., Fredrickson, C. D., Gkatzelis, G. I., Hall, S. R., Halliday, H., Hayden, K., Holmes, C. D., Huey, L. G., Jimenez, J. L., Lee, Y. R., Lindaas, J., Middlebrook, A. M., Montzka, D. D., Neuman, J. A., Nowak, J. B., Pagonis, D., Palm, B. B., Peischl, J., Piel, F., Rickly, P. S., Robinson, M. A., Rollins, A. W., Ryerson, T. B., Sekimoto, K., Thornton, J. A., Tyndall, G. S., Ullmann, K., Veres, P. R., Warneke, C., Washenfelder, R. A., Weinheimer, A. J., Wisthaler, A., Womack, C., and Brown, S. S.: Novel Analysis to Quantify Plume Crosswind Heterogeneity Applied to Biomass Burning Smoke, Environ. Sci. Technol., 55, 15646–15657, https://doi.org/10.1021/acs.est.1c03803, 2021b.

Decker, Z. C. J., Novak, G. A., Aikin, K., Veres, P. R., Neuman, J. A., Bourgeois, I., Bui, T. P., Campuzano-Jost, P., Coggon, M. M., Day, D. A., DiGangi, J. P., Diskin, G. S., Dollner, M., Franchin, A., Fredrickson, C. D., Froyd, K. D., Gkatzelis, G. I., Guo, H., Hall, S. R., Halliday, H., Hayden, K., Holmes, C. D., Jimenez, J. L., Kupc, A., Lindaas, J., Middlebrook, A. M., Moore, R. H., Nault, B. A., Nowak, J. B., Pagonis, D., Palm, B. B., Peischl, J., Piel, F. M., Rickly, P. S., Robinson, M. A., Rollins, A. W., Ryerson, T. B., Schill, G. P., Sekimoto, K., Thompson, C. R., Thornhill, K. L., Thornton, J. A., Ullmann, K., Warneke, C., Washenfelder, R. A., Weinzierl, B., Wiggins, E. B., Williamson, C. J., Winstead, E. L., Wisthaler, A., Womack, C. C., and Brown, S. S.: Airborne Observations Constrain Heterogeneous Nitrogen and Halogen Chemistry on Tropospheric and Stratospheric Biomass Burning Aerosol, Geophys. Res. Lett., 51, e2023GL107273, https://doi.org/10.1029/2023GL107273, 2024.

Dowell, D. C., Alexander, C. R., James, E. P., Weygandt, S. S., Benjamin, S. G., Manikin, G. S., Blake, B. T., Brown, J. M., Olson, J. B., Hu, M., Smirnova, T. G., Ladwig, T., Kenyon, J. S., Ahmadov, R., Turner, D. D., Duda, J. D., and Alcott, T. I.: The High-Resolution Rapid Refresh (HRRR): An Hourly Updating Convection-Allowing Forecast Model. Part I: Motivation and System Description, Weather Forecast., 37, 1371–1395, https://doi.org/10.1175/WAF-D-21-0151.1, 2022.

Elson, P., De Andrade, E. S., Hattersley, R., Campbell, E., Dawson, A., May, R., Scmc72, Little, B., Carwyn Pelley, Blay, B., Donkers, K., Killick, P., Marqh, Lbdreyer, Peglar, P., Wilson, N., Kirkham, D., Bosley, C., Signell, J., Filipe, Krischer, L., Eriksson, D., Smith, A., Carlos, McDougall, D., Crosby, A., Herzmann, D., Scaine1, Greg, and Munslowa: SciTools/cartopy: v0.17.0 (v0.17.0), Zenodo [code], https://doi.org/10.5281/ZENODO.1490296, 2018.

FIREX-AQ Science Team: Fire Influence on Regional to Global Environments and Air Quality, NASA [data set], https://doi.org/10.5067/SUBORBITAL/FIREXAQ2019/DATA001, 2019.

Fleming, Z. L., Monks, P. S., and Manning, A. J.: Review: Untangling the influence of air-mass history in interpreting observed atmospheric composition, Atmos. Res., 104–105, 1–39, https://doi.org/10.1016/j.atmosres.2011.09.009, 2012.

Freitas, S. R., Longo, K. M., Chatfield, R., Latham, D., Silva Dias, M. A. F., Andreae, M. O., Prins, E., Santos, J. C., Gielow, R., and Carvalho Jr., J. A.: Including the sub-grid scale plume rise of vegetation fires in low resolution atmospheric transport models, Atmos. Chem. Phys., 7, 3385–3398, https://doi.org/10.5194/acp-7-3385-2007, 2007.

Gargulinski, E., Halliday, H., Schwarz, J. P., Soja, A., and Wiggins, E.: FIREX-AQ Analysis and Supplementary Data, NASA [data set], https://doi.org/10.5067/ASDC/FIREXAQ_ANALYSIS_DATA_1, 2021.

Gesch, D. B., Verdin, K. L., and Greenlee, S. K.: New land surface digital elevation model covers the Earth, Eos T. Am. Geophys. Un., 80, 69–70, https://doi.org/10.1029/99EO00050, 1999.

Giangrande, S. E., Collis, S., Straka, J., Protat, A., Williams, C., and Krueger, S.: A Summary of Convective-Core Vertical Velocity Properties Using ARM UHF Wind Profilers in Oklahoma, J. Appl. Meteorol. Clim., 52, 2278–2295, https://doi.org/10.1175/JAMC-D-12-0185.1, 2013.

GOES-R Algorithm Working Group; NOAA Geostationary Operation Environmental Satellite-R Series: NOAA Geostationary Operation Environmental Satellite-R Series (GOES-R Series) Advanced Baseline Imager (ABI) Level 2 Cloud and Moisture Imagery Products (CMIP), NOAA National Centers for Environmental Information, https://doi.org/10.7289/V5736P36, 2017.

Holmes, C. D.: FIREX-AQ NOAA-CHEM Twin Otter Analysis Data, NASA [data set], https://doi.org/10.5067/ASDC/SUBORBITAL/FIREXAQ_ANALYSIS_N48_DATA_1, 2021a.

Holmes, C. D.: FIREX-AQ Satellite And Related Ancillary Data, NASA [data set], https://doi.org/10.5067/ASDC/FIREXAQ_SATELLITE_DATA_2, 2021b.

Hook, S. J., Myers, J. J., Thome, K. J., Fitzgerald, M., and Kahle, A. B.: The MODIS/ASTER airborne simulator (MASTER) — a new instrument for earth science studies, Remote Sens. Environ., 76, 93–102, https://doi.org/10.1016/S0034-4257(00)00195-4, 2001.

Karion, A., Sweeney, C., Wolter, S., Newberger, T., Chen, H., Andrews, A., Kofler, J., Neff, D., and Tans, P.: Long-term greenhouse gas measurements from aircraft, Atmos. Meas. Tech., 6, 511–526, https://doi.org/10.5194/amt-6-511-2013, 2013.

Knote, C.: icartt (2.0.0), PyPI [code], https://pypi.org/project/icartt (last access: 15 August 2020), 2022.

Lareau, N. P. and Clements, C. B.: The Mean and Turbulent Properties of a Wildfire Convective Plume, J. Appl. Meteorol. Clim., 56, 2289–2299, https://doi.org/10.1175/JAMC-D-16-0384.1, 2017.

Miller, S. D., Lindsey, D. T., Seaman, C. J., and Solbrig, J. E.: GeoColor: A Blending Technique for Satellite Imagery, J. Atmos. Ocean. Tech., 37, 429–448, https://doi.org/10.1175/JTECH-D-19-0134.1, 2020.

Mosher, F., Herbster, C., Miller, S., Zuranski, M., Sirvatka, P., Khors, R., Hoese, D., Schmit, T., Nelson, J., and Haley, R.: True-Color Imagery from GOES—A Synopsis ofPast and Present, J. Oper. Meteorol., 33–48, https://doi.org/10.15191/nwajom.2023.1104, 2023.

National Interagency Coordination Center: Incident Management Situation Report, https://www.nifc.gov/nicc/incident-information/imsr (last access: 2 November 2026), 2019.

NCEP: Upgrade NCEP Global Forecast Systems (GFS) to V15.1, Service Change Notice, 19–40, National Weather Service, https://www.weather.gov/media/notification/pdf2/scn19-40gfs_v15.1.pdf (last access: 29 July 2026), 2019.

NCEP: GFS, https://www.emc.ncep.noaa.gov/emc/pages/numerical_forecast_systems/gfs.php (last access: 29 July 2026), 2021.

Northup, E., Chen, G., Aikin, K., and Webster, C.: ICARTT File Format Standards V2.0, ESDS-RFC-029v2, NASA Earth Science Data and Information System (ESDIS) Standards Coordinating Office, https://cdn.earthdata.nasa.gov/conduit/upload/6158/ESDS-RFC-029v2.pdf (last access: 27 July 2026), 2017.

Pagonis, D., Selimovic, V., Campuzano-Jost, P., Guo, H., Day, D. A., Schueneman, M. K., Nault, B. A., Coggon, M. M., DiGangi, J. P., Diskin, G. S., Fortner, E. C., Gargulinski, E. M., Gkatzelis, G. I., Hair, J. W., Herndon, S. C., Holmes, C. D., Katich, J. M., Nowak, J. B., Perring, A. E., Saide, P., Shingler, T. J., Soja, A. J., Thapa, L. H., Warneke, C., Wiggins, E. B., Wisthaler, A., Yacovitch, T. I., Yokelson, R. J., and Jimenez, J. L.: Impact of Biomass Burning Organic Aerosol Volatility on Smoke Concentrations Downwind of Fires, Environ. Sci. Technol., 57, 17011–17021, https://doi.org/10.1021/acs.est.3c05017, 2023.

Peterson, D. A., Thapa, L. H., Saide, P. E., Soja, A. J., Gargulinski, E. M., Hyer, E. J., Weinzierl, B., Dollner, M., Schöberl, M., Papin, P. P., Kondragunta, S., Camacho, C. P., Ichoku, C., Moore, R. H., Hair, J. W., Crawford, J. H., Dennison, P. E., Kalashnikova, O. V., Bennese, C. E., Bui, T. P., DiGangi, J. P., Diskin, G. S., Fenn, M. A., Halliday, H. S., Jimenez, J., Nowak, J. B., Robinson, C., Sanchez, K., Shingler, T. J., Thornhill, L., Wiggins, E. B., Winstead, E., and Xu, C.: Measurements from inside a Thunderstorm Driven by Wildfire: The 2019 FIREX-AQ Field Experiment, B. Am. Meteorol. Soc., 103, E2140–E2167, https://doi.org/10.1175/BAMS-D-21-0049.1, 2022.

Pueschel, R. F. and Van Valin, C. C.: Cloud nucleus formation in a power plant plume, Atmos. Environ. 1967, 12, 307–312, https://doi.org/10.1016/0004-6981(78)90212-3, 1978.

Robinson, M. A., Decker, Z. C. J., Barsanti, K. C., Coggon, M. M., Flocke, F. M., Franchin, A., Fredrickson, C. D., Gilman, J. B., Gkatzelis, G. I., Holmes, C. D., Lamplugh, A., Lavi, A., Middlebrook, A. M., Montzka, D. M., Palm, B. B., Peischl, J., Pierce, B., Schwantes, R. H., Sekimoto, K., Selimovic, V., Tyndall, G. S., Thornton, J. A., Van Rooy, P., Warneke, C., Weinheimer, A. J., and Brown, S. S.: Variability and Time of Day Dependence of Ozone Photochemistry in Western Wildfire Plumes, Environ. Sci. Technol., 55, 10280–10290, https://doi.org/10.1021/acs.est.1c01963, 2021.

Rodriguez, B., Lareau, N. P., Kingsmill, D. E., and Clements, C. B.: Extreme Pyroconvective Updrafts During a Megafire, Geophys. Res. Lett., 47, e2020GL089001, https://doi.org/10.1029/2020GL089001, 2020.

Rogers, E., DiMego, G., Black, T., Ek, M., Ferrier, B., Gayno, G., Janjic, Z., Lin, Y., Pyle, M., Wong, V., Wu, W.-S., and Carley, J.: The NCEP North American Mesoscale Modeling System: Recent changes and future plans, in: 23rd Conference on Weather Analysis and Forecasting/19th Conference on Numerical Weather Prediction, 2A.4, 2009.

Ryerson, T. B., Buhr, M. P., Frost, G. J., Goldan, P. D., Holloway, J. S., Hübler, G., Jobson, B. T., Kuster, W. C., McKeen, S. A., Parrish, D. D., Roberts, J. M., Sueper, D. T., Trainer, M., Williams, J., and Fehsenfeld, F. C.: Emissions lifetimes and ozone formation in power plant plumes, J. Geophys. Res.-Atmos., 103, 22569–22583, https://doi.org/10.1029/98JD01620, 1998.

Sachse, G. W., Collins Jr., J. E., Hill, G. F., Wade, L. O., Burney, L. G., and Ritter, J. A.: Airborne tunable diode laser sensor for high-precision concentration and flux measurements of carbon monoxide and methane, Optics Electro-Optics and Laser Applications in Science and Engineering, 157, https://doi.org/10.1117/12.46162, 1991.

Saide, P. E., Thapa, L. H., Ye, X., Pagonis, D., Campuzano-Jost, P., Guo, H., Schuneman, M. L., Jimenez, J., Moore, R., Wiggins, E., Winstead, E., Robinson, C., Thornhill, L., Sanchez, K., Wagner, N. L., Ahern, A., Katich, J. M., Perring, A. E., Schwarz, J. P., Lyu, M., Holmes, C. D., Hair, J. W., Fenn, M. A., and Shingler, T. J.: Understanding the Evolution of Smoke Mass Extinction Efficiency Using Field Campaign Measurements, Geophys. Res. Lett., 49, https://doi.org/10.1029/2022GL099175, 2022.

Schwarz, J. P., Spackman, J. R., Fahey, D. W., Gao, R. S., Lohmann, U., Stier, P., Watts, L. A., Thomson, D. S., Lack, D. A., Pfister, L., Mahoney, M. J., Baumgardner, D., Wilson, J. C., and Reeves, J. M.: Coatings and their enhancement of black carbon light absorption in the tropical atmosphere, J. Geophys. Res.-Atmos., 113, 2007JD009042, https://doi.org/10.1029/2007JD009042, 2008.

Scott, S. G., Bui, T. P., Chan, K. R., and Bowen, S. W.: The Meteorological Measurement System on the NASA ER-2 Aircraft, J. Atmos. Ocean. Tech., 7, 525–540, https://doi.org/10.1175/1520-0426(1990)007<0525:TMMSOT>2.0.CO;2, 1990.

Stein, A. F., Draxler, R. R., Rolph, G. D., Stunder, B. J. B., Cohen, M. D., and Ngan, F.: NOAA's HYSPLIT Atmospheric Transport and Dispersion Modeling System, B. Am. Meteorol. Soc., 96, 2059–2077, https://doi.org/10.1175/BAMS-D-14-00110.1, 2015.

Stohl, A.: Computation, accuracy and applications of trajectories—A review and bibliography, Atmos. Environ., 32, 947–966, https://doi.org/10.1016/S1352-2310(97)00457-3, 1998.

Stohl, A., Wotawa, G., Seibert, P., and Kromp-Kolb, H.: Interpolation Errors in Wind Fields as a Function of Spatial and Temporal Resolution and Their Impact on Different Types of Kinematic Trajectories, J. Appl. Meteorol., 34, 2149–2165, https://doi.org/10.1175/1520-0450(1995)034<2149:IEIWFA>2.0.CO;2, 1995.

Tange, O.: GNU Parallel: The Command-Line Power Tool, ;login:, 36, 42–47, 2011.

Warneke, C., Schwarz, J. P., Dibb, J., Kalashnikova, O., Frost, G., Al-Saad, J., Brown, S. S., Brewer, Wm. A., Soja, A., Seidel, F. C., Washenfelder, R. A., Wiggins, E. B., Moore, R. H., Anderson, B. E., Jordan, C., Yacovitch, T. I., Herndon, S. C., Liu, S., Kuwayama, T., Jaffe, D., Johnston, N., Selimovic, V., Yokelson, R., Giles, D. M., Holben, B. N., Goloub, P., Popovici, I., Trainer, M., Kumar, A., Pierce, R. B., Fahey, D., Roberts, J., Gargulinski, E. M., Peterson, D. A., Ye, X., Thapa, L. H., Saide, P. E., Fite, C. H., Holmes, C. D., Wang, S., Coggon, M. M., Decker,

Z. C. J., Stockwell, C. E., Xu, L., Gkatzelis, G., Aikin, K., Lefer, B., Kaspari, J., Griffin, D., Zeng, L., Weber, R., Hastings, M., Chai, J., Wolfe, G. M., Hanisco, T. F., Liao, J., Campuzano Jost, P., Guo, H., Jimenez, J. L., Crawford, J., and The FIREX-AQ Science Team: Fire Influence on Regional to Global Environments and Air Quality (FIREX-AQ), J. Geophys. Res.-Atmos., 128, https://doi.org/10.1029/2022JD037758, 2023.

Washenfelder, R. A., Azzarello, L., Ball, K., Brown, S. S., Decker, Z. C. J., Franchin, A., Fredrickson, C. D., Hayden, K., Holmes, C. D., Middlebrook, A. M., Palm, B. B., Pierce, R. B., Price, D. J., Roberts, J. M., Robinson, M. A., Thornton, J. A., Womack, C. C., and Young, C. J.: Complexity in the Evolution, Composition, and Spectroscopy of Brown Carbon in Aircraft Measurements of Wildfire Plumes, Geophys. Res. Lett., 49, e2022GL098951, https://doi.org/10.1029/2022GL098951, 2022.

Xu, L., Crounse, J. D., Vasquez, K. T., Allen, H., Wennberg, P. O., Bourgeois, I., Brown, S. S., Campuzano-Jost, P., Coggon, M. M., Crawford, J. H., DiGangi, J. P., Diskin, G. S., Fried, A., Gargulinski, E. M., Gilman, J. B., Gkatzelis, G. I., Guo, H., Hair, J. W., Hall, S. R., Halliday, H. A., Hanisco, T. F., Hannun, R. A., Holmes, C. D., Huey, L. G., Jimenez, J. L., Lamplugh, A., Lee, Y. R., Liao, J., Lindaas, J., Neuman, J. A., Nowak, J. B., Peischl, J., Peterson, D. A., Piel, F., Richter, D., Rickly, P. S., Robinson, M. A., Rollins, A. W., Ryerson, T. B., Sekimoto, K., Selimovic, V., Shingler, T., Soja, A. J., St. Clair, J. M., Tanner, D. J., Ullmann, K., Veres, P. R., Walega, J., Warneke, C., Washenfelder, R. A., Weibring, P., Wisthaler, A., Wolfe, G. M., Womack, C. C., and Yokelson, R. J.: Ozone chemistry in western U.S. wildfire plumes, Sci. Adv., 7, eabl3648, https://doi.org/10.1126/sciadv.abl3648, 2021.

Yokelson, R. J., Bertschi, I. T., Christian, T. J., Hobbs, P. V., Ward, D. E., and Hao, W. M.: Trace gas measurements in nascent, aged, and cloud-processed smoke from African savanna fires by airborne Fourier transform infrared spectroscopy (AFTIR), J. Geophys. Res.-Atmos., 108, 2002JD002322, https://doi.org/10.1029/2002JD002322, 2003.